



Coupled Impacts of the Diurnal Cycle of Sea Surface Temperature on the Madden–Julian Oscillation

HYODAE SEO

Woods Hole Oceanographic Institution, Woods Hole, Massachusetts

ANEESH C. SUBRAMANIAN, ARTHUR J. MILLER, AND NICHOLAS R. CAVANAUGH

Scripps Institution of Oceanography, La Jolla, California

(Manuscript received 19 February 2014, in final form 30 June 2014)

ABSTRACT

This study quantifies, from a systematic set of regional ocean–atmosphere coupled model simulations employing various coupling intervals, the effect of subdaily sea surface temperature (SST) variability on the onset and intensity of Madden–Julian oscillation (MJO) convection in the Indian Ocean. The primary effect of diurnal SST variation (dSST) is to raise time-mean SST and latent heat flux (LH) prior to deep convection. Diurnal SST variation also strengthens the diurnal moistening of the troposphere by collocating the diurnal peak in LH with those of SST. Both effects enhance the convection such that the total precipitation amount scales quasi-linearly with preconvection dSST and time-mean SST. A column-integrated moist static energy (MSE) budget analysis confirms the critical role of diurnal SST variability in the buildup of column MSE and the strength of MJO convection via stronger time-mean LH and diurnal moistening. Two complementary atmosphere-only simulations further elucidate the role of SST conditions in the predictive skill of MJO. The atmospheric model forced with the persistent initial SST, lacking enhanced preconvection warming and moistening, produces a weaker and delayed convection than the diurnally coupled run. The atmospheric model with prescribed daily-mean SST from the coupled run, while eliminating the delayed peak, continues to exhibit weaker convection due to the lack of strong moistening on a diurnal basis. The fact that time-evolving SST with a diurnal cycle strongly influences the onset and intensity of MJO convection is consistent with previous studies that identified an improved representation of diurnal SST as a potential source of MJO predictability.

1. Introduction

The Madden–Julian oscillation (MJO) is the dominant form of intraseasonal variability in Earth's atmospheric system. Characterized by large-scale, eastward-propagating, equatorially trapped, baroclinic oscillations in the tropical wind field at periods of 30–90 days (Madden and Julian 1971, 1994), the MJO has predictability time scales of 10–30 days, far beyond the usual time scales of weather prediction (e.g., Hendon et al. 2000; Waliser et al. 2003). Although the MJO exerts a profound influence on global weather and climate

(Zhang 2005, 2013), the complexities of multiscale interaction of the circumequatorial tropical atmospheric circulation with individual cloud systems and upper-ocean processes make it difficult for the climate models to accurately represent the MJO (e.g., Zhang 2005; Madden and Julian 2005; Lin et al. 2006; Hung et al. 2013). Despite recent advancements in MJO simulation and prediction in climate and forecast models (e.g., Woolnough et al. 2007; Neale et al. 2008; K.-H. Seo et al. 2009; Seo and Wang 2010; Vitart and Molteni 2010; Subramanian et al. 2011; Kim et al. 2014), many aspects of the generation and maintenance of MJO remain elusive, such as those that are related to the initiation and intensity of MJO deep convection and the role of upper-ocean processes and air–sea interactions therein.

It is nonetheless well established that the MJO is a coupled phenomenon (Flatau et al. 1997). The upper-ocean

Corresponding author address: Hyodae Seo, Woods Hole Oceanographic Institution, 266 Woods Hole Road, MS#21, Woods Hole, MA 02543.

E-mail: hseo@whoi.edu

processes determining mixed-layer heat content, stratification, and mixing all influence the sea surface temperature (SST) and the surface heat flux; the ensuing air-sea interaction is recognized as an important element for initiation and evolution of the MJO (Waliser et al. 1999; Zhang et al. 2006). The convection and the associated winds and incident solar radiation, in turn, generate intraseasonal variations in SST. This intraseasonal SST at the same time exhibits distinctively different diurnal-scale fluctuations depending on the phases of the large-scale convection (Anderson et al. 1996). The moored observations in the western Pacific during the Tropical Ocean–Global Atmosphere Coupled Ocean–Atmosphere Response Experiment (TOGA COARE) showed enhanced amplitude of diurnal variation in SST accompanied by strong and shallow stratification during calm and sunny periods, whereas it was absent during the convectively active and windy periods (Weller and Anderson 1996).

Diurnal fluctuations of the SST and the stratification of the upper ocean influence the daily-mean and longer-time-scale SST. The one-dimensional (1D) ocean model studies by Shinoda and Hendon (1998) and Shinoda (2005) suggested that the higher daytime SST is achieved when the ocean is forced with an hourly flux in comparison to a daily-mean flux. Noting that the nighttime temperatures were similar in two cases, they suggested that the inclusion of diurnally resolved surface fluxes increases the daily-mean SST. Sui et al. (1997) suggested that the asymmetric heating of the upper ocean causes the diurnal variations in SST to influence intraseasonal SST variability. Bernie et al. (2005, 2007) confirmed this using an idealized 1D ocean model and a primitive-equation ocean general circulation model (OGCM), showing that allowing diurnal SST variations leads to amplified intraseasonal SST variations (Li et al. 2013).

By influencing intraseasonal SST, diurnally varying SST has been suggested to play an important role in MJO convection (Webster et al. 1996; Woolnough et al. 2000, 2001; Bellenger et al. 2010). Woolnough et al. (2007) compared three sets of atmospheric general circulation model (AGCM) simulations with different lower boundary conditions derived from persistent SST conditions, from an interactive OGCM with coarse vertical resolution, and from an interactive 1D model with a very high resolution (1 m) in the upper ocean. The skill was improved with the AGCM coupled to the OGCM compared to coupling with the persistent SST, but a more substantial improvement was made with the high-resolution 1D model that best resolves diurnal SST fluctuations. Bernie et al. (2008) attributed the increased intraseasonal SST variability in their coupled GCM (CGCM) to the diurnally resolved SST, which leads to

an improved MJO strength and coherency via stronger ocean–atmosphere coupling on time scales of 20–100 days. Similarly, Klingaman et al. (2008, 2011) demonstrated improved skill for northward-propagating intraseasonal oscillation due to diurnally varying SSTs.

One of the mechanisms that link diurnal SST to deep convection is through the moistening of the troposphere over warmer SST caused by the diurnal cycle. In fact, this moistening prior to convection has been well documented from TOGA COARE, showing that the detrainment from the nonprecipitating shallow cumulus and diurnal congestus clouds progressively moistens the lower to midtroposphere. This preconditioning of the local atmospheric condition is followed by a rapid moistening of the mid- to upper troposphere by deep convection (Kikuchi and Takayabu 2004; Kiladis et al. 2005; Benedict and Randall 2007; Haertel et al. 2008). The cycle of moistening and drying of the atmospheric column associated with MJO deep convection is consistent with the recharge–discharge paradigm (e.g., Bladé and Hartmann 1993; Benedict and Randall 2007).

While the link between the diurnal SST and the MJO deep convection is well established, the detailed mechanism for this link is still not clear. The previous studies used a coarse-resolution AGCM coupled to either a coarse-resolution OGCM or an idealized 1D model to assess the feedback effect. The dependence of the convection on different coupling frequencies has not been studied in a high-resolution coupled modeling framework. The case study presented in this study addresses this issue by carrying out a systematic set of high-resolution regional coupled model simulations, which will lead to a quantitative understanding of the role of diurnal SST variability in MJO convection. We target a particular MJO event observed during the Dynamics of the Madden–Julian Oscillation (DYNAMO) field experiment that took place in the central equatorial Indian Ocean from late 2011 to early 2012 (Yoneyama et al. 2013). One of the primary objectives of DYNAMO is to improve our understanding of the role of upper-ocean processes in the initiation of MJO convection. Rich in situ datasets collected from DYNAMO provide an excellent opportunity to test the capability of a regional coupled model to simulate the processes involved in MJO deep convection and hence to explore the controls of the diurnal SST cycle in the intensity of the observed MJO convection.

The paper is organized as follows. In section 2, the model and experimental designs are described. This is followed by section 3 presenting the main results of the paper. We will begin with the basic diagnostics of the simulated MJO (section 3a). The next three parts (sections 3b–d) discuss the differences in the simulated diurnal SST, surface flux, upper-ocean temperature, and

stratification. [Section 3e](#) examines the response in MJO deep convection and precipitation, and finally [section 3f](#) quantifies the convection response by a moist static energy budget analysis. A discussion and summary of the results are provided in [section 4](#).

2. Model and experiments

a. Model

We utilize the Scripps Coupled Ocean–Atmosphere Regional (SCOAR) model ([Seo et al. 2007b; <http://scoar.wikispaces.com>](#)). SCOAR currently couples one of two weather models, the Weather Research and Forecasting (WRF; [Skamarock et al. 2008](#)) Model or the Regional Spectral Model ([Juang and Kanamitsu 1994](#)), to the Regional Ocean Modeling System (ROMS; [Haidvogel et al. 2000; Shchepetkin and McWilliams 2005](#)). This study uses the WRF-ROMS version of SCOAR, taking advantage of WRF's latest physics options. The interacting boundary layer between WRF and ROMS is based on bulk aerodynamic formulas ([Fairall et al. 1996, 2003](#)) that calculate surface fluxes of momentum, turbulent and radiative heat, and freshwater based on the near-surface meteorological variables provided by WRF. ROMS is driven by these surface fluxes and, in turn, feeds back to WRF via the SST. The SCOAR model has been used in a wide range of coupled air-sea interaction studies ([Seo et al. 2006, 2007a,b, 2008a,b; H. Seo et al. 2009; Seo and Xie 2011; 2013; Putrasahan et al. 2013a,b](#)).

For the study of MJO, SCOAR is configured in a circumglobal tropical channel (see [Fig. 2a](#) for the model domain), with southern and northern boundaries at 31°S and 39°N, which are well outside the typical meridional extent of MJO ([Ray et al. 2009](#)). The horizontal resolutions in ROMS and WRF are 40 km with the matching grids and land-sea mask. For improved representation of the shallow diurnal thermocline, a large number of vertical levels are allotted in the upper ocean. For example, near the DYNAMO region in the central equatorial Indian Ocean, ROMS has 5 layers in the top 1 m and about 25 layers in the top 20 m.

A high-resolution tropical-channel regional coupled model is a unique approach to study the air-sea interaction in the tropics, allowing the circumequatorial atmospheric disturbances to freely evolve (e.g., [Ray et al. 2009, 2011](#)) and to interact with oceanic processes at high resolution. A tropical channel model approach has been often used to study the initiation and maintenance of the MJO, in which the influence from the extratropical circulations was isolated in regional ([Ray and Zhang 2010](#)) and global models ([Vitart and Jung 2010; Wedi and Smolarkiewicz 2010; Ray and Li 2013](#)). None

of these models, however, included the active ocean–atmosphere coupling; SCOAR is the first regional coupled model that includes this effect in the tropical channel configuration.

WRF uses the Zhang–McFarlane convection scheme ([Zhang and McFarlane 1995](#)) with modifications to include convective momentum transport and the dilute-plume approximation ([Neale et al. 2008](#)). This scheme is known to improve the simulation of tropical Pacific intraseasonal circulation and low-frequency variability in the National Center for Atmospheric Research (NCAR) Community Climate System Model, version 4 (CCSM4; e.g., [Subramanian et al. 2011; Zhou et al. 2012](#)). Preliminary long-term SCOAR tests showed that this scheme, run in conjunction with the University of Washington shallow cumulus convection scheme ([Park and Bretherton 2009](#)) and an updated moist boundary layer scheme by [Bretherton and Park \(2009\)](#), produces a reasonably realistic intraseasonal lead-lag relationship between SST and convection (not shown). The WRF Model is also run with the Rapid Radiation Transfer Model (RRTM; [Mlawer and Clough 1997](#)) and the Goddard scheme ([Chou and Suarez 1999](#)) for longwave and shortwave radiation transfer through the atmosphere. The Noah land surface model is used for the land surface process ([Chen and Dudhia 2001](#)).

The mixed-layer dynamics of ROMS are parameterized using a *K*-profile parameterization (KPP) scheme ([Large et al. 1994](#)). Implicit diffusivity associated with third-order upstream horizontal advection is used in the lateral plane as opposed to explicit diffusivity. The ROMS in this configuration uses [Jerlov's \(1968\)](#) optical classification of water type I, which assumes the most transparent water. The sensitivity of the result to the choice of different water types (e.g., [Shinoda 2005; Li et al. 2013](#)) is not considered in this study.

The simulation period spans 1 month from 14 November to 13 December 2011, covering both the convectively suppressed and active phases of the second MJO event during DYNAMO (hereinafter referred to as the MJO2). In the northern DYNAMO sounding array (NSA) region, defined as 0.7°S–17°N, 73°–80.5°E ([Johnson and Ciesielski 2013](#)), the former and latter periods correspond to 15–19 and 21–26 November, respectively. The NSA region is located just east of the Maldives Islands, which are known to influence the surface current and wave propagation in the equatorial Indian Ocean (e.g., [Yoon 1981; Han et al. 1999; Han 2005](#)). The Maldives are not resolved at our 40-km resolution grid, and this can influence the model–data comparison of the currents and SST in the NSA region.

We will focus on the SST, heat flux, and convection during these two 5-day periods of the suppressed and

TABLE 1. Descriptions of the experiments performed in this study.

	Description
CF1	WRF-ROMS with 1-h coupling frequency
CF3	WRF-ROMS with 3-h coupling frequency
CF6	WRF-ROMS with 6-h coupling frequency
CF24	WRF-ROMS with 24-h coupling frequency
CF1DM	WRF forced with daily-mean SST from CF1
CF1PS	WRF forced with persistent initial SST

active phases. A slight variation of the averaging period yields similar results. WRF and ROMS are initialized and driven by the atmospheric 6-hourly Interim European Centre for Medium-Range Weather Forecasts (ECMWF) Re-Analysis (ERA-Interim; [Dee et al. 2011](#)) and the daily Hybrid Coordinate Ocean Model (HYCOM) ocean analysis ([Cummings 2005](#)), respectively.

b. Experiments

To assess the influence of the presence and the amplitude of subdaily variations in SST on MJO deep convection in a coupled modeling framework, a series of SCOAR simulations are carried out with varied coupling frequency (CF) between ROMS and WRF in otherwise identical configurations (Table 1). CF is varied from 1 (CF1) to 3 (CF3) to 6 (CF6) to 24 h (CF24). Thus, in CF1, hourly-averaged atmospheric forcing and SST are exchanged, representing the best-resolved diurnal coupling, while in CF24 the daily-mean fields are interchanged, lacking the diurnal effect of the upper ocean. Besides the coupled runs, two complementary WRF-only simulations were executed to further elucidate the role of the SST in the predictability of MJO. In CF1DM, the daily-mean SST from CF1 is prescribed to WRF. Having identical daily-mean SST values, the differences between CF1DM and CF1 will reveal the impact of diurnal fluctuation in SST. In CF1PS, the persistent SST is prescribed from the initial state. Differences between CF1PS and CF1 will reveal the influence of the interactive SST featuring the preconvection warming on the MJO convection. Each of these 30-day integrations consists of five ensemble members, which are run with slightly perturbed atmospheric initial conditions. The results shown here are based on the averages of the five ensemble members. All outputs are saved at an hourly interval for each ensemble member even in those runs lacking a diurnal cycle.

3. Results

a. Simulated MJO in SCOAR

Before examining the sensitivity of the MJO2 to diurnal SST fluctuation, characteristics of the simulated

MJO in comparison to those of the observations are briefly discussed. [Figure 1a](#) shows the time-longitude diagrams of observed daily-mean precipitation anomaly (shading) from the Tropical Rainfall Measuring Mission (TRMM) satellite precipitation estimates, overlaid with 850-hPa zonal wind anomaly from the National Centers for Environmental Prediction (NCEP)-NCAR reanalysis ([Kalnay et al. 1996](#)), both of which are averaged between 10°S and 10°N. In the observations, the MJO2 event is identified as the two intense-precipitation episodes with the maximum of 2.3 mm h^{-1} at 80°E on 24 November, which propagated eastward at 8 m s^{-1} (magenta lines) as convectively coupled Kelvin waves (e.g., [Gottschalck et al. 2013](#)). The zonal wind anomalies are in quadrature with the precipitation anomaly by about 5–7 days, with the easterly (westerly) anomalies preceding (following) the peak precipitation. [Figure 1b](#) shows the eastward-propagating precipitation and wind anomalies from CF1, which qualitatively resemble the observations. CF1 shows the strong precipitation maximum at 80°E around 24–26 November, which propagated westward as a developing tropical cyclone (e.g., [Moum et al. 2014](#)). However, this is not evident in the TRMM precipitation. Zonal wind anomaly also shows greater amplitude than the NCEP.

[Figure 1c](#) shows the diagnostics of the simulated MJO as measured by the real-time multivariate MJO (RMM) index ([Wheeler and Hendon 2004](#)). The RMM index, defined as the two leading combined EOFs of outgoing longwave radiation (OLR), with zonal wind at 850 and 200 hPa in the tropics (15°S–15°N), has been widely used to assess skill of the MJO simulations and forecasts (e.g., [Waliser et al. 2009; Gottschalck et al. 2010](#)), including that for the DYNAMO period ([Gottschalck et al. 2013; Fu et al. 2013; Ling et al. 2014](#)). [Figure 1c](#) shows the trajectories of the observed (black) and simulated (CF1; red) MJO2 in the phase space for the 30-day integration period starting from 14 November 2011. In general, the RMM phase trajectory of the simulated MJO exhibits a comparable eastward-propagating feature to the observed ones, both originating from the Western Hemisphere (phase 8) and reaching the Maritime Continent (phase 5). However, the amplitudes of the simulated RMM index (normalized by one standard deviation) and the phase suggest that the simulated MJO is relatively weaker and faster than the observed one. Despite some discrepancy, the local and global characteristics of the simulated MJO reasonably resemble those from the observations. Simulating a reasonable atmospheric MJO signal in a coupled model is a primary requirement for the study of MJO-SST feedback as the SST that influences the MJO is highly dependent upon the

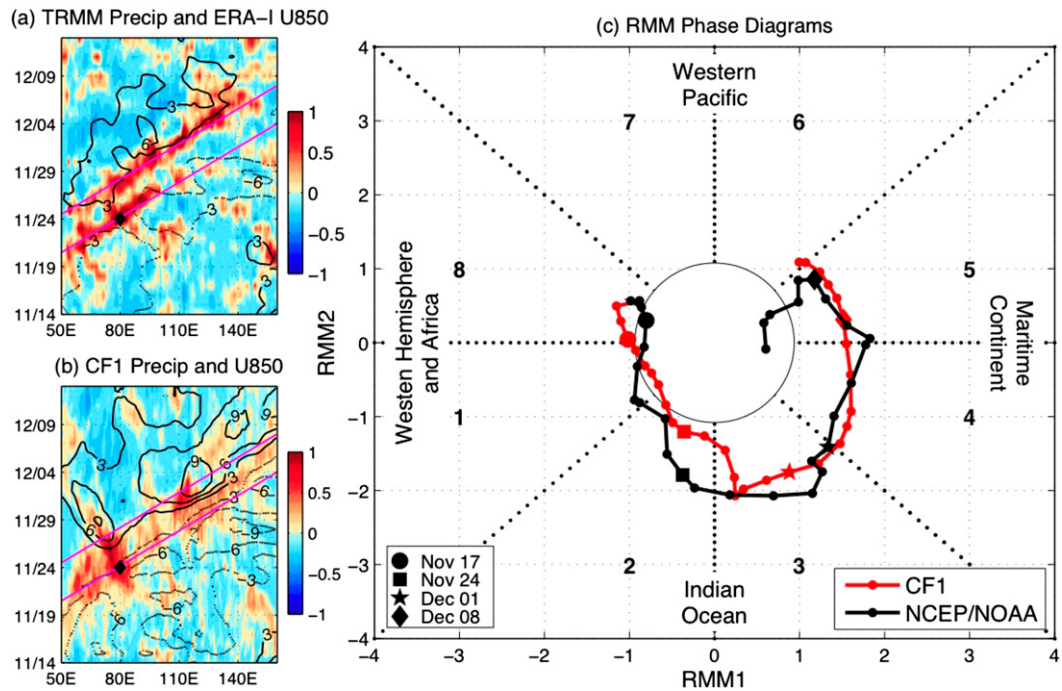


FIG. 1. (a) Time–latitude diagrams of the daily-averaged precipitation anomaly from the TRMM 3B42 estimates (shading, mm h^{-1}) and the 850-hPa zonal wind [U850; contour interval (CI) = 3 m s^{-1} , positive (negative) solid (dashed) with the zero contour suppressed] from the NCEP–NCAR reanalysis. Two magenta diagonal lines denote the 8 m s^{-1} phase lines. (b) As in (a), but from CF1. (c) RMM phase-space plot for the observations (black) and CF1 (red) for the period from 14 Nov to 13 Dec 2011. The MJO state each day is marked by filled circles while four different symbols mark 17 Nov (circles), 24 Nov (squares), 1 Dec (hexagons), and 6 Dec 2011 (diamonds).

structure and evolution of the MJO itself (Zhang and Anderson 2003).

b. Diurnal cycle in SST

Figure 2a shows the maps of amplitude of diurnal SST fluctuation (dSST) from CF1 for 15–19 November 2011, corresponding to the period before the arrival of the MJO2 deep convection in the DYNAMO region. Note that dSST is defined following Bernie et al. (2005) as the difference between the daytime maximum SST and the mean of the preceding and following nighttime minimum SSTs. According to this definition, the dSST in CF24 is not necessarily zero, although it is rather small (Table 2), as the calculation involves the nighttime minimum temperatures over two consecutive days. Regions of enhanced dSST exceeding 1°C are found in the central equatorial Indian Ocean and over the Seychelles–Chagos thermocline ridge (e.g., Li et al. 2013), which well correspond to regions of low wind speed ($<4 \text{ m s}^{-1}$), consistent with the modeling result by Shinoda et al. (2013). Figures 2b, 2d, and 2f compare the maps of dSST over the equatorial Indian Ocean, showing that dSST becomes successively weaker with less frequent coupling.

This decrease in dSST is quantified in Figs. 2c, 2e, and 2g by comparing the hourly composites of simulated SST to the observed one from the R/V *Revelle* (the green line denoting the track of the *Revelle* is identical in each panel). The *Revelle* during this period was located at 80.5°E on the equator within the broad region of high dSST. The observed dSST (Fig. 2c, black curve) for this period is about 1.30°C , with an SST peak at 1500 local time (LT). The observed dSST is underestimated in CF1 (0.73°C) when sampled at the location of the *Revelle*, representing 56% of the observed range. It is possible that our unusually high vertical resolution in the upper ocean and hourly sampling is still insufficient to accurately represent the observed dSST. However, previous studies by Bernie et al. (2005) showed that 90% of the observed dSST can be captured by the vertical resolution in the upper ocean of 1 m and the surface fluxes of temporal resolution of 3 h. The diminished dSST would be more likely due to stronger surface wind speed in the model (2.4 m s^{-1}) than what was observed from the *Revelle* (1.8 m s^{-1}). This strong wind bias, not present in the ERA-Interim, acts to erode the diurnal warm layer. However, the comparison of dSST among the SCOAR coupled runs clearly illustrates that dSST becomes

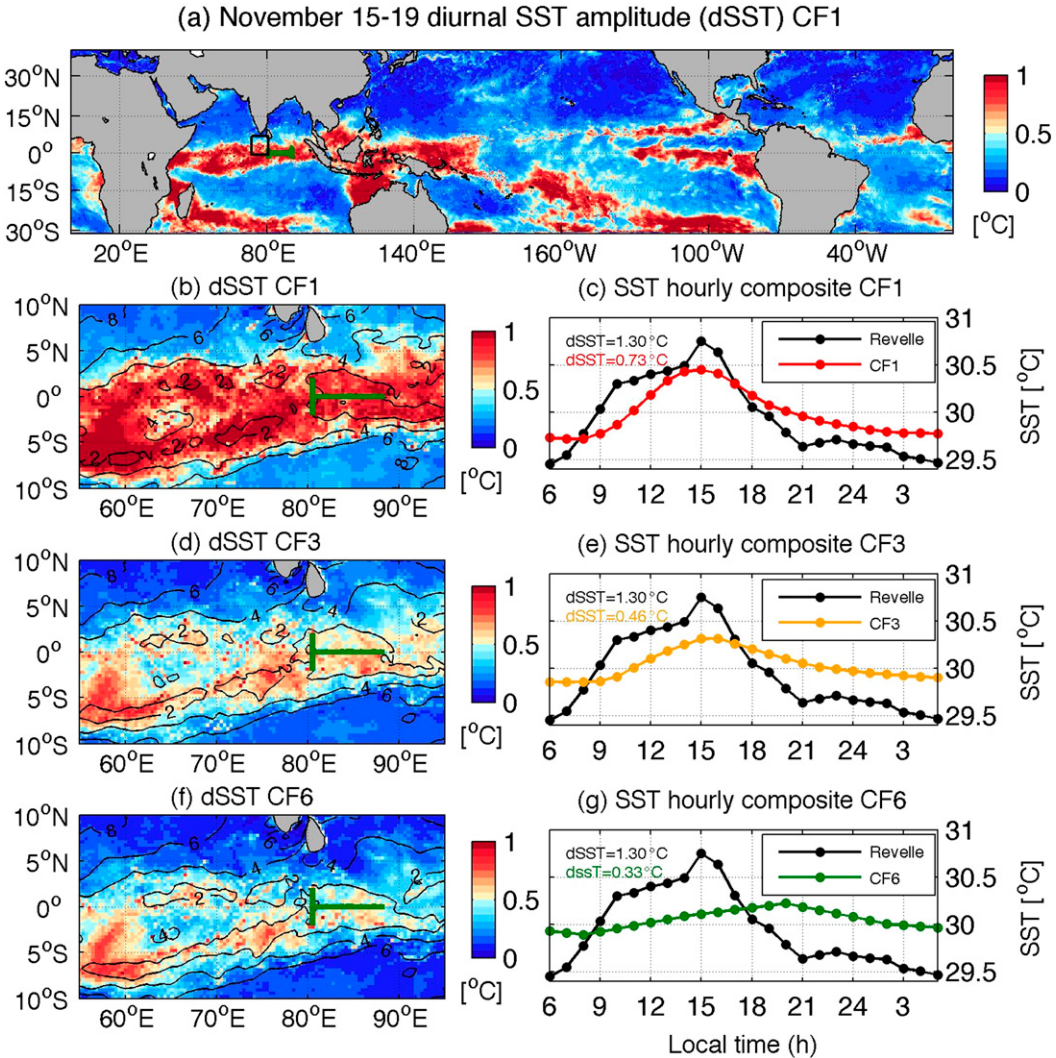


FIG. 2. (a),(b),(d),(f) Maps of diurnal SST amplitude (dSST), defined as the difference between the daytime maximum SST and the mean of the preceding and following nighttime minimum SSTs, overlaid with the mean 10-m wind speed (contours; CI = 2 m s^{-1}) for the period of 15–19 Nov 2011. The green line denotes the track of the R/V *Revelle*. The black box in (a) encompasses the region of the northern sounding array (NSA), 0.7°S – 7°N , 73° – 80.5°E , during DYNAMO by Johnson and Ciesielski (2013). (c),(e),(g) Hourly composites of SST corresponding to (b),(d),(f), respectively, in comparison to the observed one from the R/V *Revelle* (black).

successively weaker as the CF increases from 1 to 3 h (0.46°C) and then to 6 h (0.33°C).

The comparison between the model and observations was so far at a single point location. To better represent the broad-scale convection processes observed in the DYNAMO region, we will be focusing on the NSA region, in which the MJO signal was strongest, to examine the convection as measured from the sounding arrays during DYNAMO (Johnson and Ciesielski 2013). As these sounding observations were routinely assimilated into the ERA-Interim, the convection represented therein over the NSA region should be of high quality.

Lack of diurnally resolved SST in the NSA, however, led us to compare the simulated NSA SSTs with those from the *Revelle*, located in the eastern end of the NSA. Figure 3a compares the hourly *Revelle* SST time series with the simulated NSA SST during the MJO2 period. The observed SST (black curve) shows a period of enhanced warming accompanied by large diurnal fluctuations between 15 and 19 November and a transition to cooling and reduced diurnal cycle between 22 and 26 November. Figures 3b and 3c present the hourly SST composites during these two periods. Again, the observed dSST in the suppressed phase is 1.30°C with

TABLE 2. Mean SST ($^{\circ}$ C) and diurnal amplitude of SST ($^{\circ}$ C) from the R/V *Revelle* and each model simulation averaged over the NSA region for the suppressed and active phases of MJO2 and their difference.

	Suppressed phase (15–19 Nov)		Active phase (22–26 Nov)		Suppressed minus active	
	Mean SST	dSST	Mean SST	dSST	Mean SST	dSST
Revelle	29.95	1.30	29.20	0.49	0.75	0.81
CF1	29.81	0.58	29.42	0.19	0.39	0.39
CF3	29.73	0.39	29.45	0.13	0.28	0.26
CF6	29.72	0.29	29.44	0.13	0.28	0.16
CF24	29.73	0.03	29.56	0.03	0.17	0

a mean SST of 29.95° C, which are both reduced to 0.49° and 29.20° C, respectively, in the active phase (Table 2). Reduced dSST during the active phase implies that the diurnal SST is likely not important for the feedback to the atmosphere during this phase.

The simulated SST qualitatively resembles the observed change in dSST and the cooling trend in the mean

SST (Table 2). However, the excessively high SST from the model after 27 November toward the end of the simulation period is striking, which might be related to two deficiencies in the ocean–atmosphere process associated with the simulated MJO. First, the model lacks the observed two wind events associated with the MJO2 but instead shows one broad peak (Fig. 1). Observations from Moum et al. (2014) suggest that the mixed-layer depth deepened and SST cooled further after the second wind event. Thus, lack of this second wind event might have contributed to the lack of significant cooling and thus to the warm bias. Furthermore, the clearest water type used in the ocean model might allow a buildup of excessive subsurface warm anomaly during the suppressed phase (as is discussed in section 3c), which then would be entrained to the surface layer during the wind event. This will reduce the amplitude of SST cooling. Given the discrepancy in simulated and observed SSTs after the MJO2, we will limit our analysis to the first half of the time series,

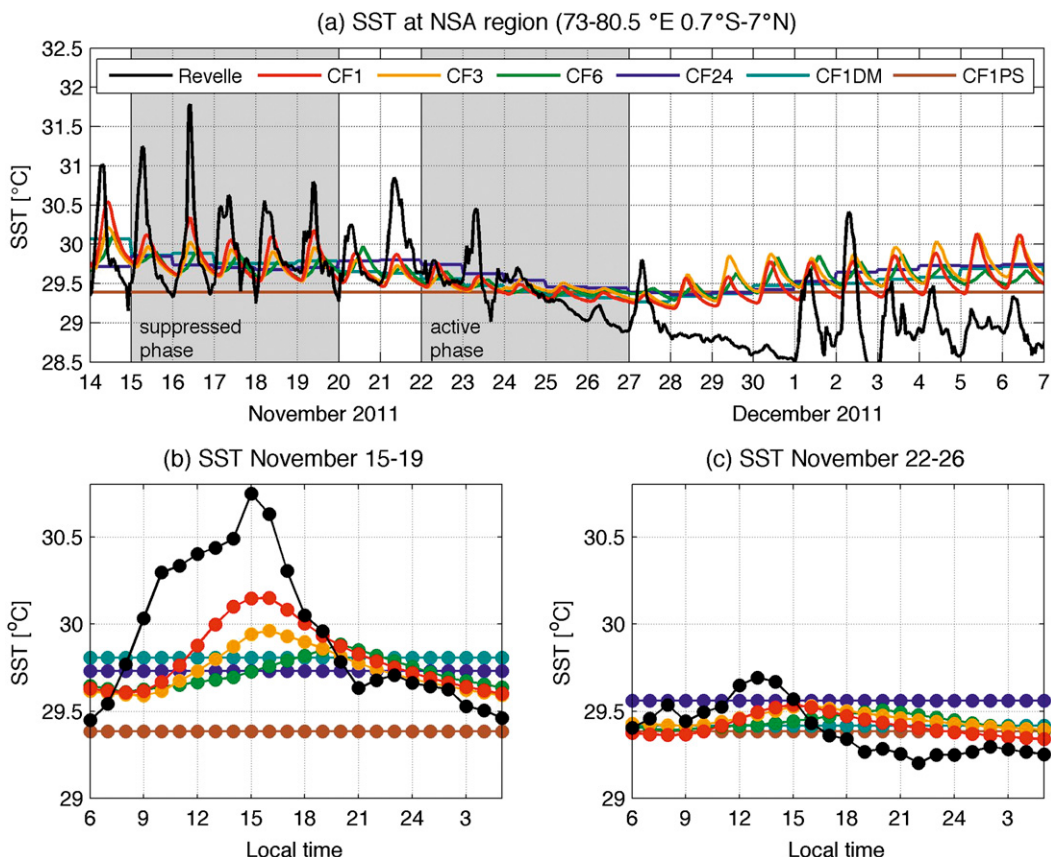


FIG. 3. (a) The hourly time series of the observed SST from the R/V *Revelle* (black) and the simulated SSTs (sampled following the *Revelle*), color coded to represent the different experiments. The gray boxes mark the two time periods, the convectively suppressed phase of the MJO2 (15–19 Nov 2011) and the active phase (22–27 Nov 2011). (b),(c) The hourly composites SSTs calculated for each time period.

which includes periods of both suppressed and active convection.

With the largest dSST, CF1 also shows the highest mean SST (29.81°C) during the suppressed phase in comparison to CF3–CF24 showing approximately 29.72° – 29.73°C . A two-sided Student's *t* test indicates that the SST difference between CF1 and the rest of the coupled runs (CF3–CF24) is significant at $p = 1\%$ confidence level. The higher mean SST in CF1 by approximately 0.1°C indicates that the diurnal SST cycle enhances the daily-mean SST, which is consistent with previous studies showing a higher mean SSTs ($\sim 0.1^{\circ}\text{C}$) with subdaily forcing (e.g., [Bernie et al. 2007](#); [Li et al. 2013](#)). [Shinoda and Hendon \(1998\)](#) using the 1D ocean model, showed an even greater SST difference (0.2° – 0.5°C) with and without diurnal variation of shortwave radiation in the western tropical Pacific. The mean SST from CF1DM is identical to that of CF1 but has no dSST by definition. CF1PS has a cooler SST lacking the preconvection warming. The subsequent impact on the surface flux and the atmospheric convection is discussed in the following sections.

In the transition from the suppressed to the active phase, the SST from the *Revelle* is cooled by 0.75°C ([Table 2](#)), which is in line with the typical SST change associated with MJO of 0.25° – 0.3°C , but often reached up to 1°C in the western Pacific ([Weller and Anderson 1996](#)). The SST cooling of 0.39°C in CF1 is reasonable in comparison to such observations. The SST cooling in CF1 is greater than other runs by more than 0.1°C ([Table 2](#)) and especially in comparison to CF24 by 0.22°C . This might be related to the stronger heat loss by LH ([Table 3](#)). This suggests that the SST cooling associated with the passage of the MJO convection might be reinforced by the preconvection diurnal SST, which is congruent with the studies by [Bernie et al. \(2005\)](#) and [Li et al. \(2013\)](#) showing the amplified intraseasonal SST in response to MJO with a greater diurnal SST.

c. Diurnal cycle in latent heat flux

During the suppressed phase, the higher SST in CF1 than CF6 and CF24 occurs despite the larger evaporative cooling. [Figure 4a](#) shows the hourly evolution of the latent heat flux (LH; positive upward) in the NSA as well as the observed daily LH estimate from objectively analyzed air-sea fluxes (OAFlux; [Yu and Weller 2007](#); black curve). The hourly time series clearly shows the LH at this location evolves in association with the arrival of MJO2, with reduced heating of the atmosphere during the suppressed phase and amplified heating during the active phase ([Table 3](#)). During the suppressed phase, the diurnal amplitude in LH (dLH), defined in the same

TABLE 3. Time-mean latent heat flux (W m^{-2}) and diurnal amplitude of latent heat flux (W m^{-2}) over the NSA region during the suppressed and active phases of MJO2 from the OAflux and model simulations; dLH from OAflux is not available.

	Suppressed phase of MJO2 (15–19 Nov)		Active phase of MJO2 (22–26 Nov)	
	Mean LH	dLH	Mean LH	dLH
OAflux	95.9	N/A	142.3	N/A
CF1	103.8	30.2	169.2	40.1
CF3	97.4	24.6	168.3	51.6
CF6	98.0	21.1	148.6	28.9
CF24	97.7	30.2	160.6	49.9
CF1DM	101.2	29.8	165.3	44.8
CF1PS	79.3	25.3	91.0	26.0

way as dSST, is proportional to dSST, with the highest dLH in CF1, 30.2 W m^{-2} , and the lowest in CF6, 24.6 W m^{-2} . This leads to a mean LH of 147.8 W m^{-2} in CF1, higher than those of CF3–CF24, showing 140 – 142 W m^{-2} . This difference in LH between CF1 and other less frequently coupled runs is significant at $p = 1\%$ level. The peak LH difference between CF1 and CF24 can be up to 20 W m^{-2} ([Fig. 4](#)). [Schiller and Godfrey \(2005\)](#) suggested from a diagnostic 1D model that the ocean loses heat additionally by 10 W m^{-2} due to diurnal variation of SST. The errors in LH and the net surface heat flux (Q_{net}) due to the omission of dSST ([Clayson and Bogdanoff 2013](#)) were estimated to be approximately 6 – 8 W m^{-2} in the equatorial Indian Ocean during the boreal winter. The time-mean difference in Q_{net} between CF1 and CF24 is 9.9 W m^{-2} , consistent with their estimates. Differences of heat flux of this size would have nonnegligible impact on atmospheric physical processes ([Kawai and Wada 2007](#)).

The dLH in CF24, despite the lack of dSST, is greater (30.2 W m^{-2}) than those of CF3 and CF6 and comparable to that of CF1. This large dLH without dSST is also seen in CF1DM, forced with daily-mean SST from CF1, and CF1PS, forced with the time-invariant initial SST ([Table 3](#)). This is because in these runs the dLH was determined predominantly by the diurnal variations in surface wind speed. In the bulk parameterization, latent heat flux is expressed as $LH = \rho L C_H W10(q_s - q_a)$, where ρ is the density of air, L is the latent heat of vaporization of water, C_H is the bulk exchange coefficient, $W10$ is the wind speed at 10 m , q_s is the saturation specific humidity at the temperature of the ocean surface, and q_a is the specific humidity of air at 2 m . The diurnal variation in LH is determined jointly by that of $W10$, q_s , and q_a . The hourly composites of each of these quantities are plotted in [Fig. 5](#). $W10$ in all cases shows the peak at 0900–1000 LT, with q_s peaking at 1500–1600 LT and q_a near local midnight. Hence, the morning peak in LH

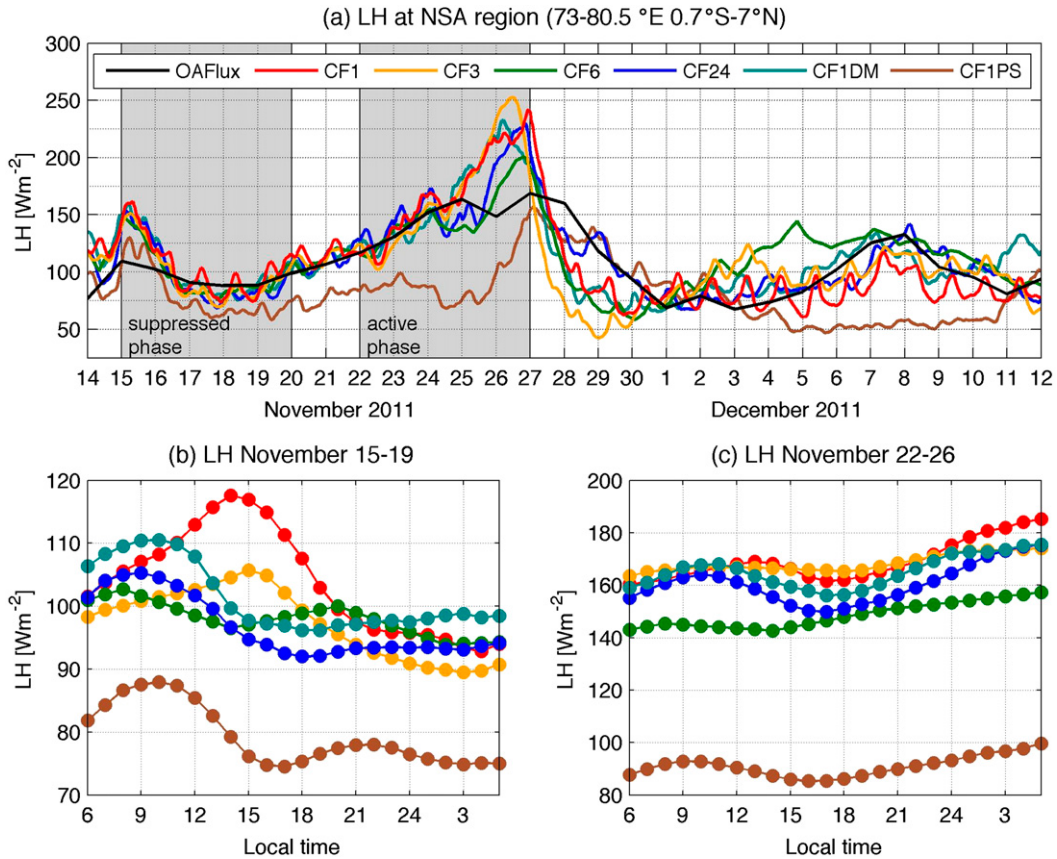


FIG. 4. (a) Simulated time series of LH (W m^{-2} ; positive upward) averaged over the NSA region (0.7°S – 7°N , 73° – 80.5°E), color coded to represent the different experiments. (b),(c) The hourly composites of LH calculated for suppressed and active phase of MJO2, respectively.

apparent in CF24, CF1DM, and CF1PS is due to that of W10 in the absence of strong diurnal q_s , which is strongly influenced by diurnal SST. This is in marked contrast to CF1 where the diurnal q_s plays a leading role in locating the peak in LH at 1400 LT, despite a significant peak in W10 in the morning. The diurnal q_a is evidently weak, so its late night peak is not apparent in that of LH. This suggests that the diurnal cycle in SST plays a pivotal role in locating the diurnal peak in LH at the time of diurnal maxima of SST and q_s , thus maximizing the moistening of the atmosphere. Observations in the western Pacific during TOGA COARE indicate the initiation of the shallow convection activity occurred in the afternoon at the time of the SST and surface air temperature maxima (e.g., Chen and Houze 1997; Johnson et al. 1999). A recent modeling study (Thayer-Calder and Randall 2009) based on the superparameterized Community Atmosphere Model (SP-CAM) suggests the importance of the lower-tropospheric moistening during the suppressed phase for the MJO convection. The current study shows that this diurnal moistening of the atmosphere might be

erroneously represented if the model lacks or under-represents the SST diurnal cycle.

In summary, there are at least two effects of the diurnal SST variation on LH and the moistening of the troposphere. First, the diurnal SST increases the daily-mean SST and LH via a rectified upper-ocean response. Second, given the same time-mean SST, the diurnal SST also enhances the diurnal moistening process by collocating the diurnal peak in LH with those of SST and q_s . The subsequent sections will discuss the relative importance of the two effects on the MJO convection and precipitation.

d. Diurnal evolution of the upper-ocean temperatures

Figures 6a–c compare the evolution of the upper-ocean temperature anomalies (the 30-day mean is removed) in the NSA along with the hourly time series of anomalous zonal wind at 10 m (U10; blue) and downward shortwave radiation (SWD; red). In all cases (CF3 is not shown), the suppressed phase is characterized by a weak easterly anomaly and a positive SWD anomaly, leading to warming of the upper ocean with sharp diurnal

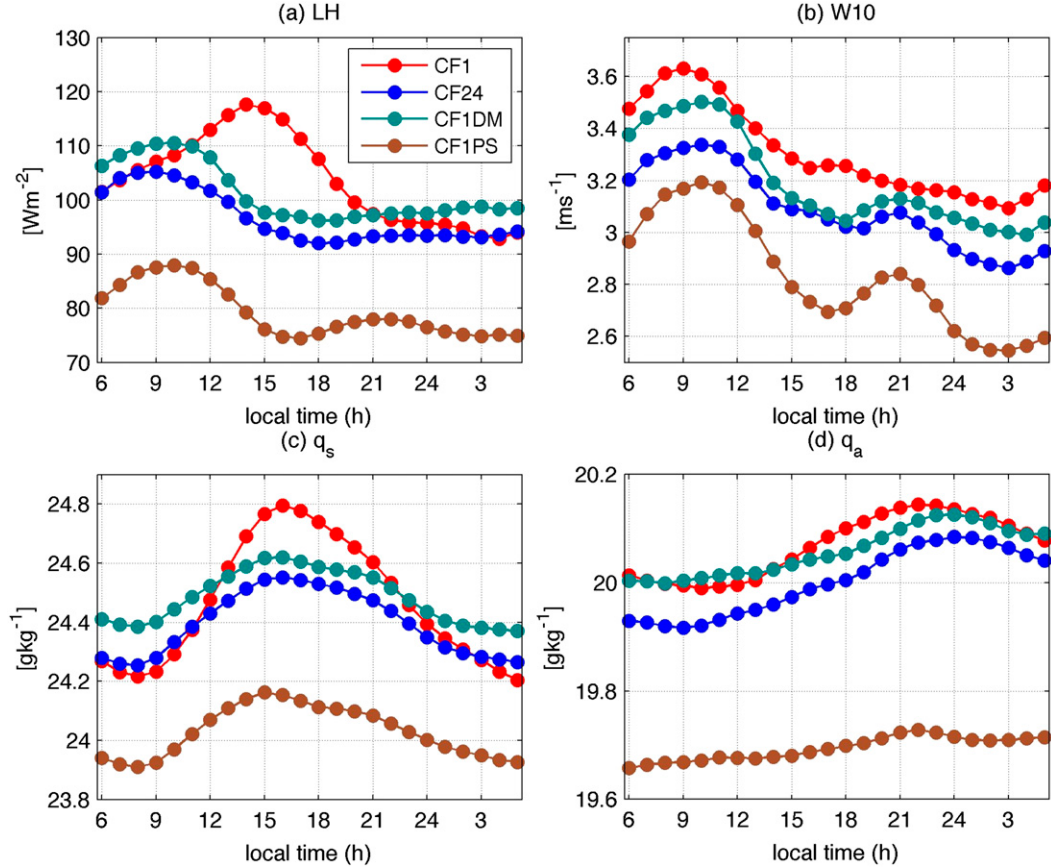


FIG. 5. The hourly composites of (a) latent heat flux (W m^{-2}), (b) 10-m wind speed (m s^{-1}), (c) saturation specific humidity at the temperature of the ocean surface (g kg^{-1}), and (d) the specific humidity of air at 2 m (g kg^{-1}) during the suppressed phase of MJO2.

thermocline and shoaled turbulent boundary layer (TBL; gray line). The thickness of the diurnal warm layer, as inferred from the daytime TBL depth, is less than 2 m in CF1 but gets deeper as the CF increases (3 m in CF6 and 7 m in CF24; not shown). As the TBL marks the depth to which the surface-driven turbulent mixing penetrates (e.g., Large et al. 1994), the thin daytime TBL indicates that the incident solar radiation retained within the surface layer effectively raises the SST on a diurnal basis and increases the heat transfer to the atmosphere as latent heat (Fig. 4). The pronounced upper-ocean warming anomaly ($>0.3^\circ\text{C}$) below the TBL, reaching greater than 20-m depth in CF1 and evidently less so in CF6 and CF24, is due to the penetration of shortwave radiation flux through the TBL, reinforcing the stable upper-ocean stratification (e.g., Shinoda and Hendon 1998). The thin and warm daytime TBL is deepened at night due to surface radiative cooling and enhanced turbulent mixing in the upper ocean (Yoneyama et al. 2013; Moum et al. 2014). After 23 November, the SST cools as the TBL deepens in

association with the negative SWD anomaly, signaling the arrival of the MJO2 deep convection. The extent to which the TBL deepens is greater in CF1 than in CF6 and CF24, suggesting that the shear instability in the mixed layer would also play an important role in enhancing the cooling in CF1 (Moum et al. 2014). The zonal wind switches to the westerly and strengthens until 27 November, with the maximum upper-ocean cooling during 28–30 November.

Clearly, the upper-ocean warming during the suppressed phase is more pronounced and reaches deeper in CF1 than in CF6 and CF24. The diurnal cycle in the upper-ocean temperature is also strongest in CF1. This difference is further illustrated in Figs. 6d–f, which compare the time-mean profiles of the upper-ocean temperature during the suppressed phase. Error bars represent the respective intradiurnal standard deviation, which is simply the standard deviation of hourly temperature composites. The enhanced diurnal variability in the upper 5 m is stronger in CF1 than in CF6. The time means of both the SST and the top-5-m temperature are higher during this period in CF1, as are the diurnal

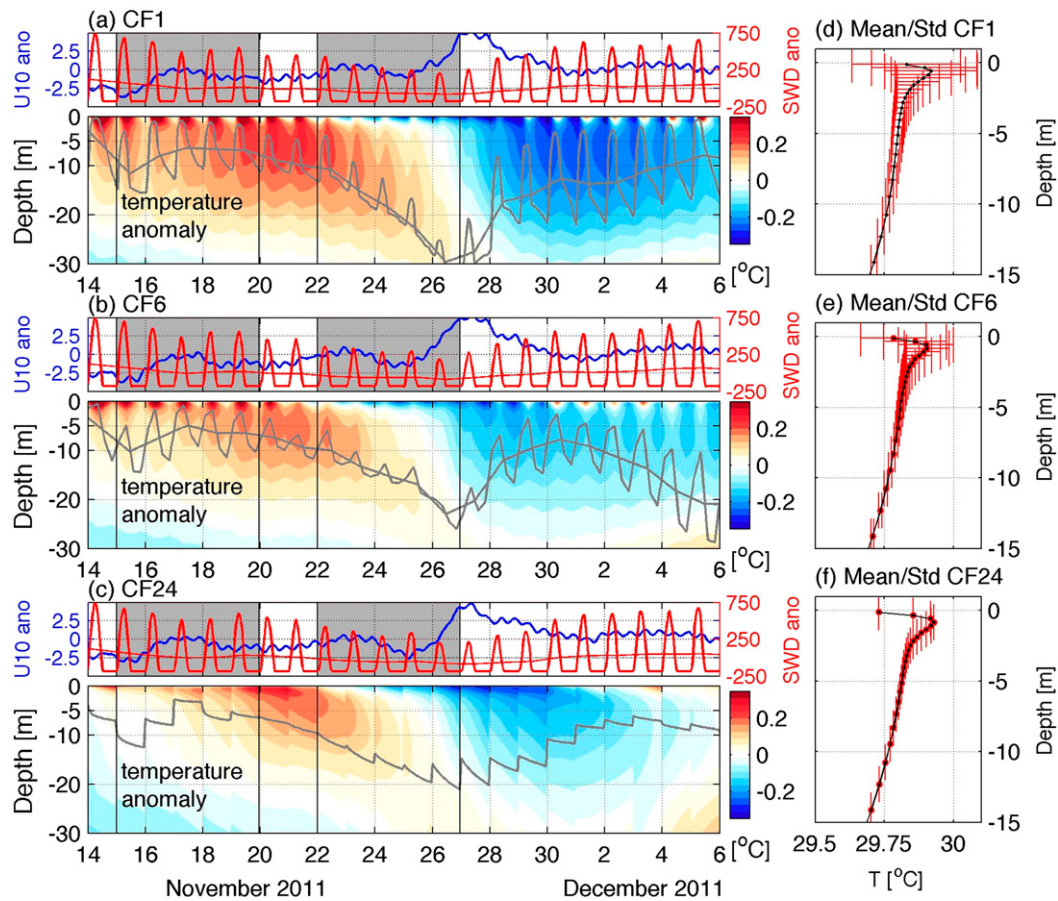


FIG. 6. (left) Time–depth diagrams of the upper-ocean temperature anomalies (shading, $^{\circ}\text{C}$) averaged over the NSA region (0.7°S – 7°N , 73° – 80.5°E) from (a) CF1, (b) CF6, and (c) CF24, overlaid with the respective depth of turbulent boundary layer (TBL; m, gray contours). Both the hourly- and daily-mean TBL values are shown in (a) and (b). Blue and red lines denote the anomalous 10-m zonal wind (m s^{-1}) and the downward shortwave radiation at the surface (W m^{-2}), respectively. The anomalies are with respect to the 30-day mean. (right) The mean upper-ocean temperature profiles for (d) CF1, (e) CF6, and (f) CF24 are overlaid with ± 1 intradiurnal standard deviation (STD) for the suppressed phase of MJO2 (14–21 Nov 2011).

variations (Table 4), in comparison to CF6 and CF24. The greater range of diurnal variation in the upper-ocean temperature and SST thus helps the sea surface reach a higher daytime temperature in CF1.

e. Impact on MJO deep convection and precipitation

How is the SST condition related to the MJO2 deep convection? Figure 7 shows the time–longitude diagrams of the observed and simulated daily-mean precipitation anomalies averaged between 10°S and 10°N . Figure 8 compares the time series of the daily-mean total precipitation amount averaged over the NSA region. During the suppressed phase, the observed precipitation amount was small (Fig. 7a and black line in Fig. 8) but increases to the maximum on 24 November followed by the secondary peak on 27 November. The period after 29 November marks another suppressed phase before

the so-called MJO3 (Moum et al. 2014). The simulated precipitation from both the coupled and uncoupled models shows the eastward-propagating precipitation that qualitatively resembles the observations.

The maximum precipitation amount in the coupled runs is found on 25–26 November (Fig. 8b). If the initiation of the simulated MJO is defined as the timing of the peak convection [see Straub (2013) for a definition of the MJO initiation], then the initiation is not noticeably different among the coupled runs (i.e., CF1–CF24). However the intensity of convection shows noticeable proportionality to the preconvection dsST; that is, the average precipitation amount gets smaller as the coupling becomes less frequent. Figure 8b confirms this by showing that CF1 (red) on average has the largest amount of precipitation (1.72 mm h^{-1} ; Table 5), compared to CF3 (1.63 mm h^{-1}), CF6 (1.51 mm h^{-1}), and

TABLE 4. Time-mean and intradiurnal standard deviation (STD), defined as the standard deviation of the hourly composites, of the SST ($^{\circ}$ C) and the top-5-m averaged temperature ($^{\circ}$ C) during the suppressed phase of MJO2 over the NSA region.

	CF1	CF6	CF24
SST: mean \pm STD	29.8 ± 0.30	29.8 ± 0.16	29.7 ± 0.00
5-m temperature:	29.9 ± 0.24	29.9 ± 0.15	29.9 ± 0.00
mean \pm STD			

CF24 (0.93 mm h^{-1}). The precipitation difference between CF1 and the rest of the coupled runs (CF3–CF24) is significant at 1% level according to a two-sided Student's *t* test. Therefore, there appears to be a systematic intensity response of precipitation associated with MJO2 to the preconvective dSST, suggesting a possible causal (lead–lag) relationship between the two.

The average precipitation in CF1 is only slightly higher than that in CF1DM during the active phase

despite the lack of a diurnal SST cycle in CF1DM (Table 5). Furthermore, the precipitation amount from CF1DM is higher than that of CF3–CF24. This implies that, of the two primary effects of diurnal SST—raising the time-mean SST/LH and strengthening the diurnal moistening process—the former plays the dominant role in enhancing convection and precipitation. CF1PS has a delayed peak in precipitation on 27 November unlike the observations and CF1, suggesting that the lack of preconvective warming and moistening lowers the predictive skill of the onset of convection.

Figures 9 and 10 illustrate the evolution of vertical structure of the atmosphere over the NSA. Figure 9a shows the specific humidity anomaly q' (with respect to the 30-day mean) overlaid with the pressure vertical velocity anomaly ω' from the ERA-Interim. Figure 10a shows the temperature anomaly T' and the zonal wind anomaly U' . The observed evolution is compared with the two model runs showing the clearest contrast, CF1

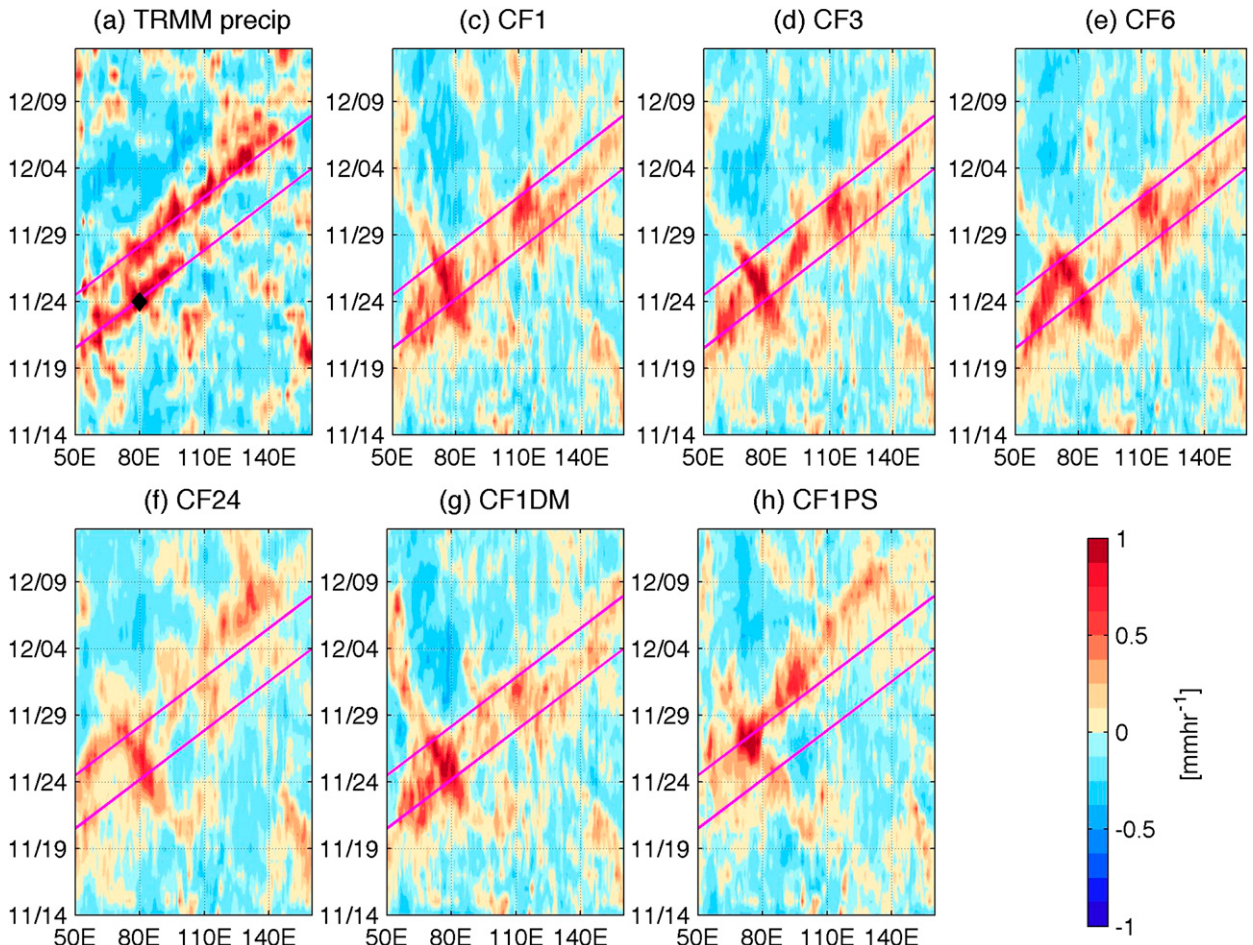


FIG. 7. Time–longitude diagrams of daily-mean precipitation rate anomaly (mm h^{-1}) averaged over 10°S – 10°N from (a) TRMM 3B42, (b) CF1, (c) CF3, (d) CF6, (e) CF24, (f) CF1DM, and (g) CF1PS. Two magenta diagonal lines, common to all the panels, denote the 8 m s^{-1} phase lines derived from (a).

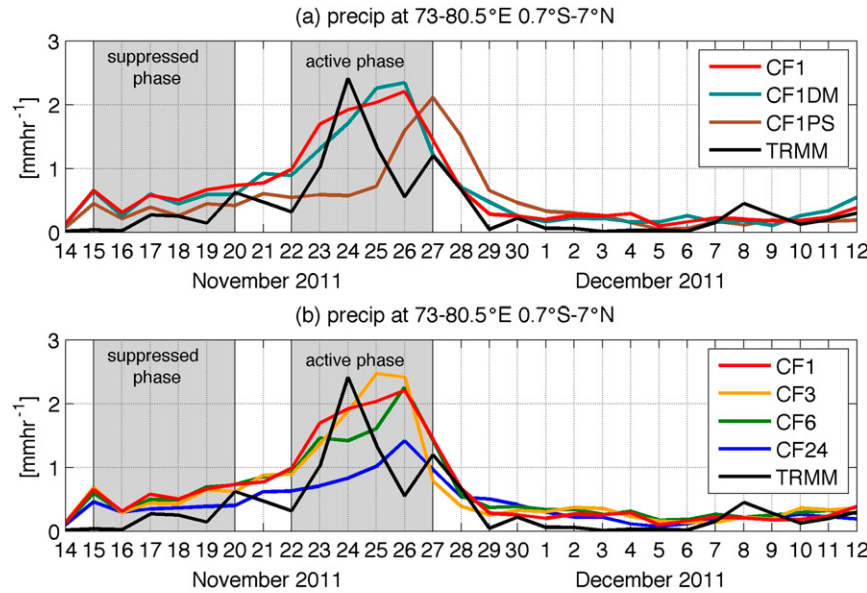


FIG. 8. Time series of daily-mean total precipitation rates (mm h^{-1}) over the NSA region (0.7°S – 7°N , 73° – 80.5°E) of (a) CF1, CF1DM, CF1PS, and TRMM, and (b) CF1, CF3, CF6, CF24, and TRMM. The gray boxes delineate the periods of the convectively suppressed (15–19 Nov 2011) and active (20–26 Nov 2011) phases of MJO2.

and CF24. In the ERA-Interim, the suppressed phase is dominated by drying of the low to midtroposphere (bluish shading in Fig. 9a) with the anomalous subsidence (red contours). This period is accompanied by an easterly (westerly) wind anomaly at the lower (upper) level showing a baroclinic vertical structure (Fig. 10a). A moistening of the lower atmosphere (1000–850 hPa) is seen from 18 November accompanied by the strengthened low-level easterlies. The evolution of the moistening appears to be gradual when area-averaged, although previous observations at single locations suggest a stepwise evolution of the moisture fields (e.g., Kikuchi and Takayabu 2004; Del Genio et al. 2012). The simulated moisture evolution, if sampled at a single location (e.g., the Gan Island), captures the gross feature of the stepwise evolution (not shown) observed from DYNAMO (Johnson and Ciesielski 2013). The moistening peaks during 24–26 November in the midtroposphere (500–600 hPa) result from the upward moisture transport marked by the strong ascending motion at -15 hPa h^{-1} . The resultant mid- to upper-tropospheric heating at 600–300 hPa (Fig. 10a) instigates the onset of low-level westerly and upper-level easterly winds. This time–height structure of the atmosphere associated with the MJO is consistent with the observations during DYNAMO (Johnson and Ciesielski 2013) and TOGA COARE (e.g., Kiladis et al. 2005), showing the moistening of the low to midtroposphere by detrainment from the shallow

cumulus and congestus and the moistening of the mid- to upper troposphere by deep convection.

The CF1 qualitatively well represents this well-documented evolution. The troposphere is anomalously dry with strong large-scale subsidence and low-level (upper level) easterly (westerly) wind during the suppressed phase. The moistening of the midtroposphere and warming of the upper troposphere during the active convection is accompanied by strong rising motion and the onset of low-level westerly wind. There is a hint that the moistening occurs in the initially dry lower troposphere, although it occurs at a higher level (600–700 hPa) than what ERA-Interim suggests. The warming and moistening during the suppressed phase imply the development of shallow convection. Of course, a model at this resolution cannot explicitly resolve shallow cumulus or diurnal congestus, but their effects on the moistening of the atmosphere are included through the parameterizations of the turbulent boundary layer and the shallow cumulus convection in the WRF Model. The fact that the time-mean LH is enhanced and that dLH is proportional to dSST lends strong support to the notion that this moistening originates from the surface through

TABLE 5. Average rainfall amount (mm h^{-1}) during the active phase of MJO2 (22–26 Nov 2011).

	TRMM	CF1	CF3	CF6	CF24	CF1DM	CF1PS
Rainfall	1.14	1.72	1.63	1.51	0.93	1.62	1.02

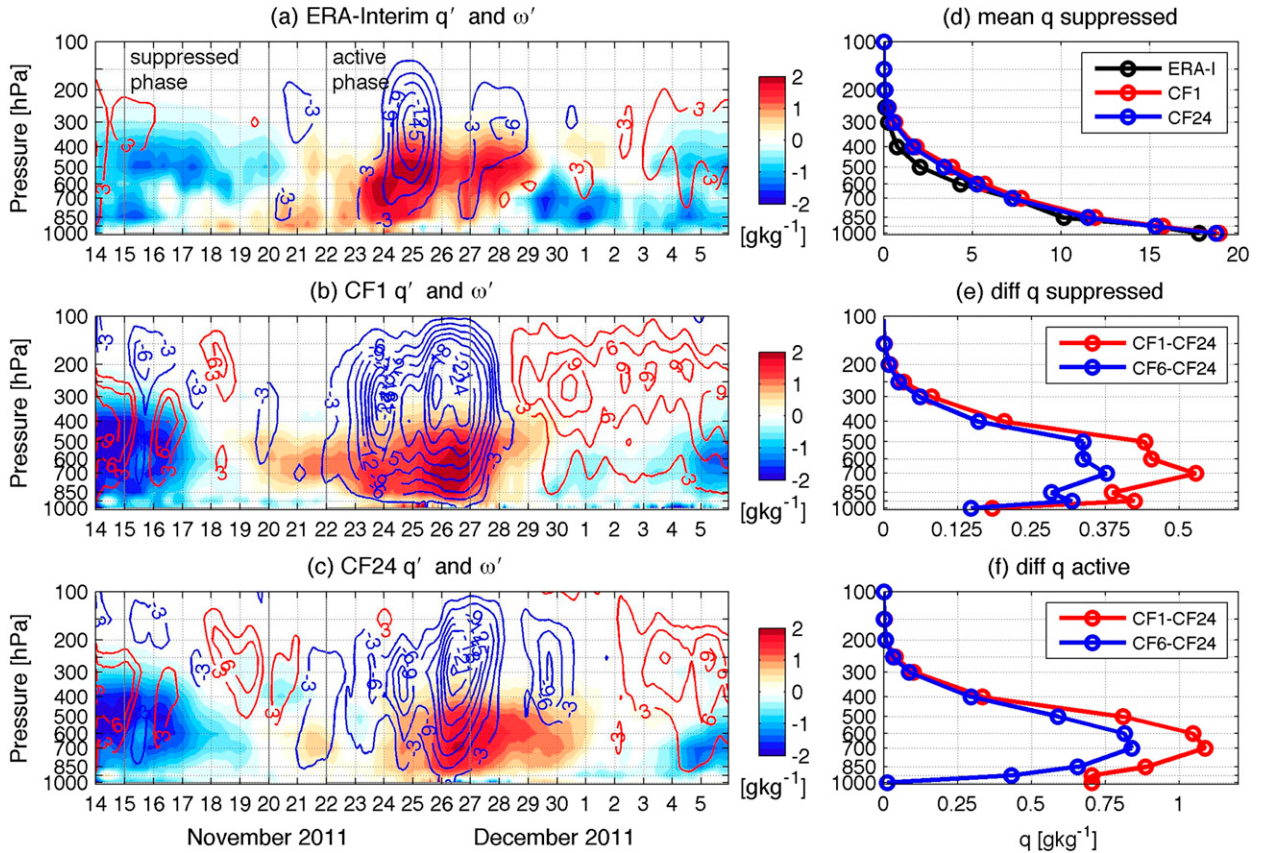


FIG. 9. Pressure–time cross sections of the anomalous specific humidity (q' ; g kg^{-1}) over the NSA region (0.7°S – 7°N , 73° – 80.5°E) from (a) ERA-Interim, (b) CF1, and (c) CF24. The anomalies are respect to the 30-day-mean values. Contours denote the pressure velocity anomaly (ω' ; $\text{CI} = 10 \text{ hPa } \text{h}^{-1}$) with the blue (red) representing the ascending (descending) motion. (d) The time-mean specific humidity profiles during the suppressed phase of MJO2. Also the differences in the mean specific humidity are shown for the (e) suppressed and (f) active phases.

enhanced latent heating over higher mean SST and dSST. The low-level moistening leading to the deep convection can have contributions from both the lateral advection (Benedict and Randal 2009; Maloney 2009; Kiranmayi and Maloney 2011) and the local vertical advection from LH release from the ocean (Maloney and Sobel 2004; Maloney 2009). As will be clarified in the next subsection, it is the latter that plays the leading role in this case.

Comparing CF1 and CF24, Figs. 9 and 10 clearly show that the ascending motion, the upper-level warming, and the midlevel moistening during the active convection are all stronger in CF1 than in CF24. This suggests that evolution of the convection is generally amplified with a stronger diurnal SST that leads to the higher time-mean SST via a rectified upper-ocean response. The mean vertical distribution of q and T shows that the atmosphere is moister (Fig. 9e) and warmer (Fig. 10e) at the low to midlevels in CF1 than in CF6 and even more so than in CF24 during the suppressed phase. Consequently, the stronger deep convection leads to greater

midlevel moistening and upper-level warming in CF1 during the active phase (Figs. 9f, 10f). The time–height evolution in CF1DM is quite similar to those of CF1 (not shown), indicating that the primary effect of diurnal SST on the convection and precipitation is by raising the time-mean SST and LH. As Slingo et al. (2003) suggested, the diurnal cycle in SST might cause the shallow convection in the suppressed phase of the MJO, whereby the cumulus congestus clouds moisten the free troposphere. This preconditioning by the local diurnal cycle in SST for the MJO deep convection occurs in the current model predominantly through the diurnal cycle in SST raising time-mean SST and latent heat flux.

f. Column-integrated moist static energy budget analysis

To further elucidate the process relating the diurnal cycle in SST to the intensity of MJO convection, a column-integrated moist static energy (MSE) budget analysis (Maloney 2009) has been executed. This can be cast as

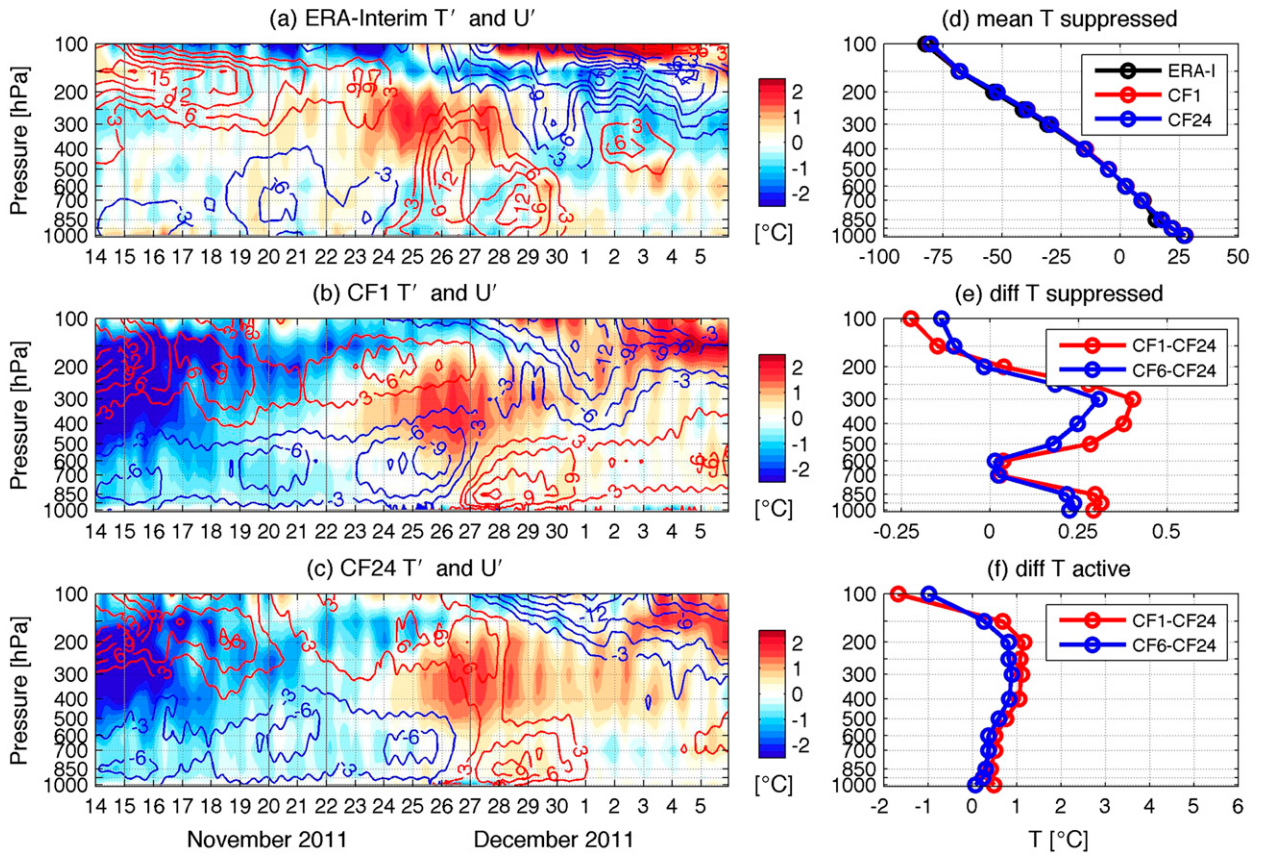


FIG. 10. As in Fig. 9, but for temperature anomaly (T' , colors; $^{\circ}\text{C}$) and zonal wind anomaly (U' , contours; $\text{CI} = 3 \text{ m s}^{-1}$). The red (blue) contours denote westerly (easterly) wind anomalies.

$$\underbrace{\langle h_t \rangle}_{\text{Tendency}} = \underbrace{\langle -v_h \nabla h \rangle}_{\text{Horizontal advection}} + \underbrace{\langle -\omega h_p \rangle}_{\text{Vertical advection}} + \underbrace{\langle \text{LH} + \text{SH} \rangle}_{\text{Turbulent heat flux}} + \underbrace{\langle \text{LW} + \text{SW} \rangle}_{\text{Longwave and shortwave heating rate}} + \underbrace{R}_{\text{Residual}},$$

where the subscripts denote partial derivatives. In this equation, h is the MSE, defined as $h = c_p T + gz + Lq$, where c_p is the specific heat at constant pressure, T is temperature, z is height, g is the gravitational acceleration, L is the latent heat of vaporization at 0°C , and q is the specific humidity. LH and SH represent the surface latent and sensible heat fluxes, and LW and SW are the longwave and shortwave heating rate. The residual R includes processes not considered (e.g., latent heat due to fusion) or captured (by hourly sampling) in this analysis and errors due to discretization and vertical interpolation of the model grids (e.g., Kiranmayi and Maloney 2011). The angle brackets denote column integration from 1000 to 100 hPa. The column-integrated tendency of MSE $\langle h_t \rangle$ is balanced by the column-integrated import or export of MSE by horizontal and vertical advection, the longwave and shortwave heating,

and the turbulent heat fluxes. As the longwave and shortwave heating rates were not saved at every vertical level, these terms are lumped together with the residual in this analysis. Given previous studies suggesting the importance of longwave heating in the MSE budget (e.g., Andersen and Kuang 2012; Arnold et al. 2013), the lack of an estimate for $\langle \text{LW} + \text{SW} \rangle$ is a caveat of the result provided here.

Figure 11a compares the individual budget terms during the suppressed phase, color coded to represent different experiments. Among the coupled SCOAR simulations (CF1–CF24), there is an overall increasing tendency in the column-MSE recharge with the decreasing CF. The exception to this trend is between CF3 and CF6, but their difference is small and perhaps insignificant. The contribution from the horizontal and vertical advection is negative and negligible. Zonal

(meridional) advection is positive (negative) with amplitude of 30 W m^{-2} (not shown); the two components thereby cancel each other. In contrast, the turbulent heat flux ($\text{LH} + \text{SH}$, where LH is dominant), which is proportional to dSST, is the only dominant source term that accounts for the more expedited rate of MSE recharge with the more frequent coupling. The dominant role of $\text{LH} + \text{SH}$ in the buildup of MSE at this stage is also consistent with the result from ERA-Interim (not shown). While $\langle \text{LW} + \text{SW} \rangle$ and R together slow the recharge rate, this is not the dominant factor. Thus, the greater dSST helps to achieve a greater release of LH to the atmosphere, leading to the more rapid buildup of MSE. Examining the uncoupled simulations, each of the MSE budget terms in CF1DM has comparable magnitude to those in CF1, despite the very different diurnal cycle in LH between CF1 and CF1DM. This confirms that the dominant effect of the diurnal SST variation on the MJO convection is through raising time-mean SST and LH. In CF1PS, with time-invariant SST lacking preconvective heating and moistening, the MSE recharge is noticeably slower than CF1DM and CF1, since LH is smaller.

Once the large-scale MJO convective system arrives in the NSA (Fig. 11b), $\langle h_t \rangle$ becomes small, and a balance develops between the MSE export by the vertical advection and, to a lesser extent, by horizontal advection and the MSE import by $\text{LH} + \text{SH}$ and $\langle \text{LW} + \text{SW} \rangle + R$, which are of comparable magnitude. The magnitudes of vertical advection among the coupled runs exhibit a good proportionality to dSST. Therefore, the preconditioned atmosphere by higher SST and dSST is conducive to a locally more intensified deep convection.

The column-integrated moisture budget analysis (not shown) reinforces this finding; that is, during the suppressed phase, the moisture gain through the negative apparent moisture sink by surface evaporation is more important than the moisture loss by the drying associated with the convective downdrafts. During the active phase, a balance is established between the increased export of moisture by the deep convection and the moisture gain by surface evaporation.

A further decomposition of the column-integrated vertical advection term, $\langle -\omega h_p \rangle$, highlights the difference in diurnal moistening process. With ω and h_p decomposed into the daily mean (overbars) and the diurnal deviation from the daily mean (primes), the total vertical advection can be expressed as $\langle -\omega h_p \rangle = \langle -\bar{\omega} h_p \rangle + \langle -\omega' h'_p \rangle$, where $\langle -\omega' h'_p \rangle$ represents the non-linear rectification effect by ω' and h'_p . The cross-product terms are negligible. Figure 12a shows that, during the suppressed phase, the daily-mean advection, $\langle -\bar{\omega} h_p \rangle$, exports the MSE by the large-scale convective

downdrafts producing anomalously dry, cold air (Figs. 9 and 10), with amplitude showing no obvious proportionality to dSST. The import of the column-integrated MSE is through the diurnally rectified vertical advection, $\langle -\omega' h'_p \rangle$, which nearly cancels the export by $\langle -\bar{\omega} h_p \rangle$ and scales quasi-linearly with dSST and $\langle \text{LH} + \text{SH} \rangle$. The greatest MSE import is in CF1 on a diurnal scale, which then subsides with increasingly infrequent coupling. During the active phase, the deep convection is dominated by the daily-mean vertical advection. This analysis is qualitatively consistent with Haertel et al. (2008), who suggested based on the MSE budget analysis of the TOGA COARE sounding data that the vertical advection by shallow convection supports the convergence of MSE prior to the MJO deep convection. Note that $\langle -\omega' h'_p \rangle$ in CF1DM, despite no dSST, is only slightly weaker than that in CF1 ($42 \text{ vs } 37 \text{ W m}^{-2}$), which is due to the pronounced diurnal cycle in LH that is dominated by that in W10. The same is true with CF1PS showing more than half of $\langle -\omega' h'_p \rangle$ in CF1 despite the lack of dSST.

Therefore, the column-integrated MSE and moisture budget analyses suggest that, as in the observations (e.g., Waliser et al. 1999; Kemball-Cook and Weare 2001; Raymond et al. 2003; Stephens et al. 2004), the moisture in the lower atmosphere is accumulated over the warm SST during the calm and sunny period. The resulting increase in the column MSE facilitates deep convection, a process consistent with the recharge–discharge paradigm [e.g., Bladé and Hartmann 1993; see also Xu and Rutledge (2014) for DYNAMO observations]. In this study, the diurnal SST plays a pivotal role in enhancing the daily-mean latent heat flux, and to a less extent anchoring the diurnal peak of the latent heat flux with that of SST and q_s . This is consistent with some previous studies suggesting the leading role of the latent heat flux in the development of the deep convection and the recharge–discharge process (Maloney et al. 2010; Sobel et al. 2008). The result, however, is at odds with other studies suggesting the essential role of horizontal advection (Maloney 2009). The importance of longwave heating associated with the reduced outgoing longwave radiation over the warm SST suggested from recent SP-CAM studies (Andersen and Kuang 2012; Arnold et al. 2013) cannot be thoroughly assessed in this study.

4. Summary and discussion

One of the overarching goals of the DYNAMO field experiment is to assess whether and how upper-ocean processes such as the barrier layer, mixing, and stratification influence the MJO initiation by affecting the mixed-layer temperature, SST, and air-sea flux (Yoneyama et al. 2013).

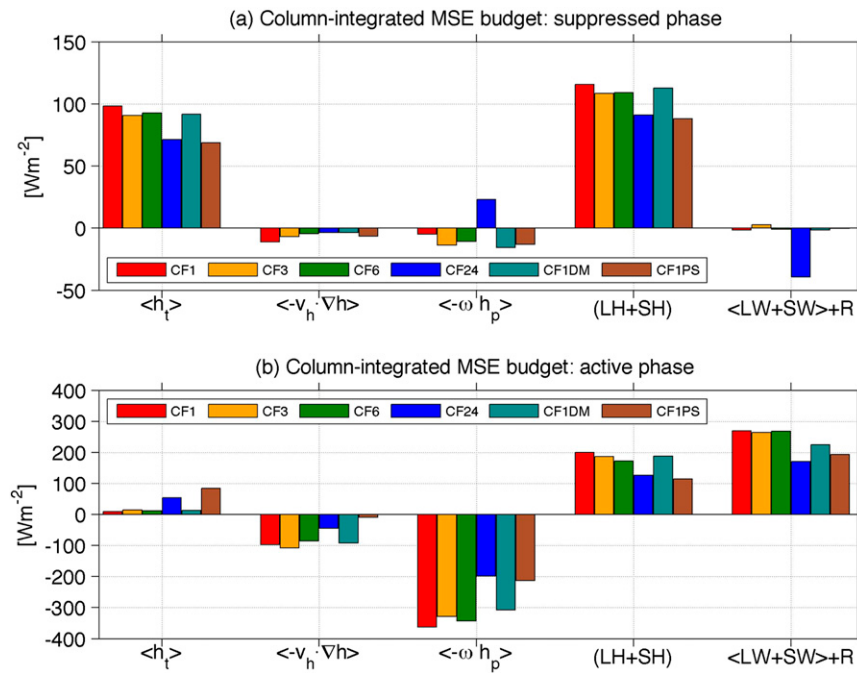


FIG. 11. The column-integrated MSE budget terms, color coded to represent the results from different experiments, during the (a) suppressed (15–19 Nov 2011) and (b) active (22–26 Nov 2011) phases of MJO2. All quantities are averaged in the NSA region (0.7°S – 7°N , 73° – 80.5°E).

These oceanic properties exhibit a pronounced diurnal variation during the calm and sunny period prior to MJO deep convection. The resultant warm SST by a nonlinear rectification effect moistens the local atmosphere and influences the ensuing deep convection. The purpose of this study is to identify the leading mechanism(s) by which diurnal SST variability influences the atmosphere during DYNAMO.

The SCOAR regional coupled model was constructed targeting the November 2011 MJO event in a tropical-channel configuration at 40-km resolution, with unusually high vertical resolution in the upper ocean, and with 1-hourly model coupling frequency (CF). All these factors are designed to better capture the evolution of the oceanic and atmospheric processes associated with the passage of MJO so as to test their sensitivity to the diurnal SST variation. CF is varied in an otherwise identical configuration from 1 to 24 h. As the differences among the runs with varied CF can be due to a different mean state, two complementary WRF-only simulations were executed forced with the daily-mean SST from CF1 (CF1DM) and with the persistent initial SST (CF1PS) in order to test the role of interactive SST in the timing and intensity of MJO.

WRF uses the modified Zhang–McFarlane deep convection scheme in conjunction with the University of Washington shallow cumulus scheme (Park and

Bretherton 2009). The use of deep and shallow convection scheme, in combination with the interactive ocean, is instrumental for the improved simulation of the lower- and upper-level moistening process in our model. This is consistent with the result from a previous WRF modeling study by Hagos et al. (2011), who suggest that WRF can produce a reasonable MJO only if the representation of the moisture variability is improved via moisture nudging. In their study, the moisture nudging enforces the realistic moistening and stratiform heating process prior to the active MJO, leading to improved simulation of MJO. In our study, this effect is included by the diurnal SST and the shallow convection scheme.

During the suppressed phase, the more frequent coupling leads to a stronger dSST and a higher mean SST. The daily-mean SST is significantly higher (by 0.1°C) in CF1 than in CF24, despite a higher latent heat loss by 10 W m^{-2} in the time mean and up to 20 W m^{-2} on a diurnal time scale. The LH diurnal cycle in CF1 is determined by that of the saturation water vapor mixing ratio at the sea surface q_s peaking in the afternoon, as does the SST. In cases with weak (CF6) or no (CF24 and CF1DM) diurnal SST, in contrast, the diurnal peak in LH corresponds to that of surface wind speed occurring in the morning. The associated dLH in CF24 and CF1DM is comparable to that of CF1 despite this very

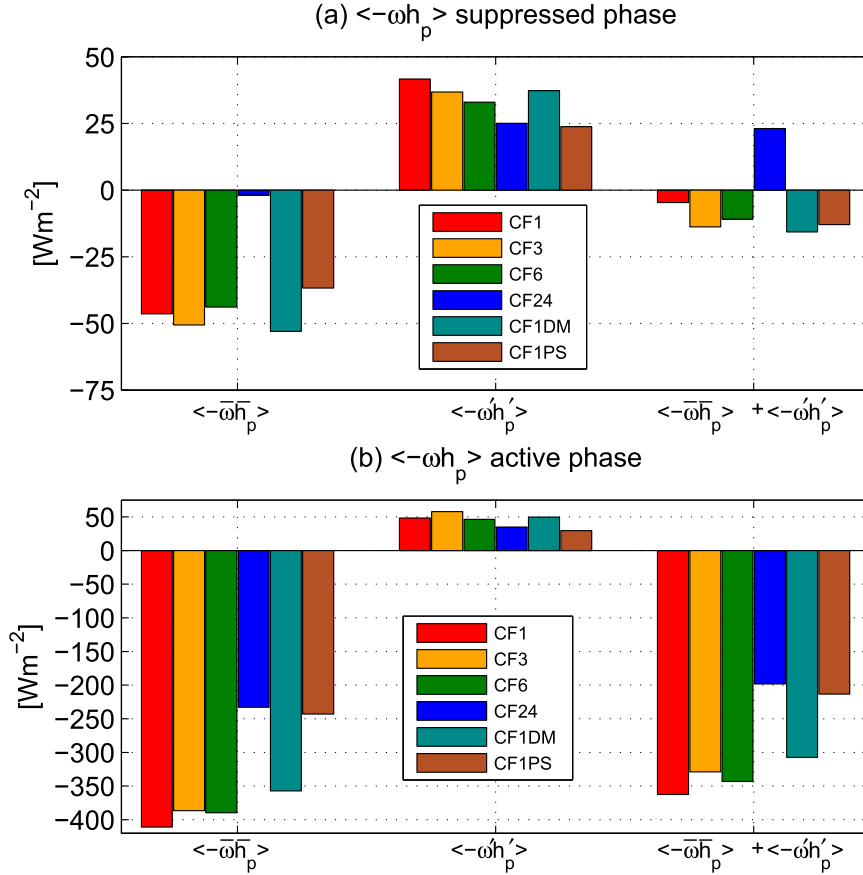


FIG. 12. As in Fig. 11, except showing the breakdown of the total vertical advection of the column-integrated MSE $\langle -\omega m_p \rangle$ into the daily-mean advection $\langle -\bar{\omega} m_p \rangle$ and the contribution by the nonlinear rectification $\langle -\omega' m'_p \rangle$.

different diurnal fluctuation. However, the mean LH is greater in CF1 compared to CF24, suggesting the importance of diurnal moistening in the troposphere. The two effects of diurnal SST (i.e., the increased time-mean SST/LH and the enhanced diurnal peak of LH) yield statistically significant response in the intensity of the convection; that is, the precipitation amount during the active phase is greater in CF1 than in CF24. The difference in time-mean LH and precipitation between CF1 and CF1DM is small despite the lack of dsST in CF1DM, which implies that the diurnal variation of SST and LH is of secondary importance to the convection. The primary effect of including diurnal SST, hence, is to raise the daily-mean SST and LH, which enhance deep convection. Among the SCOAR coupled runs in which the dsST scales with the CFs, the resultant rainfall amount is quite reasonably proportional to preconvection mean SST and dsST.

The relationship is further quantified by a column-integrated moist static energy (MSE) budget analysis. The recharge rate of the column MSE during the

suppressed phase is stronger with more frequent coupling. The latent heat flux is the dominant source term. The net vertical advection plays a minor role during this period, but the decomposition of this term reveals the diurnal moistening process. The daily-mean advection exports the MSE, slowing down the recharge via the convective downdrafts, which is almost cancelled by the import of MSE by the vertical advection due to a diurnal rectification effect. While the former is not related to the diurnal SST, the latter shows a clear linear relationship with the CFs, suggesting that the MSE import by vertical advection on a diurnal basis is associated with the diurnal cycle in SST and LH.

Comparison of the result between CF1 and two WRF-only simulations highlights the role of interactive and diurnal SST on the predictability of MJO convection. As the model was initialized approximately 1 week before the onset of the convection, which is shorter than the typical MJO predictability time scale (Waliser et al. 2003), some predictability is provided by the initial condition. In addition to this initial predictability, time-varying lateral

and the SST boundary conditions appear to strongly influence the skill of simulating MJO2 with the current SCOAR model, especially the intensity and timing of the peak convection. Previous extensive tests using the tropical-channel WRF Model (Ray et al. 2009) suggested the critical role of time-varying lateral boundary conditions, which allowed meridional advection of the westerly momentum from the extratropics. Other factors such as detailed characteristics of SST, model physics, and horizontal resolutions did not noticeably improve the simulation of the MJO (Ray et al. 2009; 2011). This study is partly consistent in that the CF1PS with a time-varying lateral boundary condition without evolving SST is able to produce the MJO-related signal. The timing of the peak convection in CF1PS, however, was delayed 1–2 days compared to the case that allowed the time-varying SST (CF1DM) or that allowed the diurnal SST (CF1). This indicates that the SST warming prior to the convection was critical for predicting the timing of MJO convection in the current model. Allowing diurnal variability of SST in CF1–CF24 did not shift the timing of the MJO convection or significantly alter the propagation characteristics; nonetheless it influenced the intensity of the local convection significantly. Further study of MJO predictability, including the comparison of the existing runs with the one without meridional lateral boundary influence (e.g., Ray et al. 2009), will clarify the predictability source of the MJO2 convection in a regional coupled modeling framework. This is a topic of an ongoing study.

Overall, this study sought to quantify from a systematic set of regional coupled model simulations the effect of diurnal SST variability on the onset and intensity of MJO convection. The result of this study, while limited to one particular MJO event during DYNAMO, presents a valuable insight into the physical process by which diurnal SST variability influences the MJO convection. Despite the underestimation of the observed diurnal-cycle amplitude in the present model, the result shows a robust proportionality of the intensity of deep convection to the mean and diurnal variation in SST. The result also reveals the significant role of the time-varying and diurnally fluctuating SST in the predictive skill of MJO. The diurnal evolution in SST regulated by the ocean–atmosphere coupling is thus important for MJO convection by influencing the latent heat flux (Sobel et al. 2008). The current study, therefore, provides consistent results from the previous studies (e.g., Bernie et al. 2007; Woolnough et al. 2007) that identified an improved representation of diurnally evolving SST as the potential source of the MJO predictability. The diurnal variations in mixing and stratification in the upper ocean, important for diurnal SST variations, are crudely

represented in many global-scale models. A high-resolution regional coupled model such as SCOAR and other existing ones (e.g., Shinoda et al. 2013) can potentially improve on both process and predictive understanding of the MJO–ocean interactions on diurnal to intra-seasonal time scales.

Acknowledgments. The authors gratefully acknowledge support from the Office of Naval Research (N00014-13-1-0133 and N00014-13-1-0139) and National Science Foundation EaSM-3 (OCE-1419235). HS especially thanks the Penzance Endowed Fund for their support of Assistant Scientists at WHOI. Authors also thank Raghu Murtugudde, Markus Jochum, Duane Waliser, and three anonymous reviewers for their constructive comments, which helped to substantially improve the manuscript. The DYNAMO datasets were obtained from the NCAR EOL web site at http://data.eol.ucar.edu/master_list/?project=DYNAMO. This work used the Extreme Science and Engineering Discovery Environment (XSEDE), which is supported by National Science Foundation (OCI-1053575).

REFERENCES

- Andersen, J. A., and Z. Kuang, 2012: Moist static energy budget of MJO-like disturbances in the atmosphere of a zonally symmetric aquaplanet. *J. Climate*, **25**, 2782–2804, doi:[10.1175/JCLI-D-11-00168.1](https://doi.org/10.1175/JCLI-D-11-00168.1).
- Anderson, S. P., R. A. Weller, and R. Lukas, 1996: Surface buoyancy forcing and the mixed layer of the western Pacific warm pool: Observations and 1D model results. *J. Climate*, **9**, 3056–3085, doi:[10.1175/1520-0442\(1996\)009<3056:SBFATM>2.0.CO;2](https://doi.org/10.1175/1520-0442(1996)009<3056:SBFATM>2.0.CO;2).
- Arnold, N. P., Z. Kuang, and E. Tziperman, 2013: Enhanced MJO-like variability at high SST. *J. Climate*, **26**, 988–1001, doi:[10.1175/JCLI-D-12-00272.1](https://doi.org/10.1175/JCLI-D-12-00272.1).
- Bellenger, H., Y. N. Takayabu, T. Ushiyama, and K. Yoneyama, 2010: Role of diurnal warm layers in the diurnal cycle of convection over the tropical Indian Ocean during MISMO. *Mon. Wea. Rev.*, **138**, 2426–2433, doi:[10.1175/2010MWR3249.1](https://doi.org/10.1175/2010MWR3249.1).
- Benedict, J., and D. A. Randall, 2007: Observed characteristics of the MJO relative to maximum rainfall. *J. Atmos. Sci.*, **64**, 2332–2354, doi:[10.1175/JAS3968.1](https://doi.org/10.1175/JAS3968.1).
- , and —, 2009: Structure of the Madden–Julian oscillation in the superparameterized CAM. *J. Atmos. Sci.*, **66**, 3277–3296, doi:[10.1175/2009JAS3030.1](https://doi.org/10.1175/2009JAS3030.1).
- Bernie, D., S. Woolnough, J. Slingo, and E. Guilyardi, 2005: Modeling diurnal and intraseasonal variability of the ocean mixed layer. *J. Climate*, **18**, 1190–1202, doi:[10.1175/JCLI319.1](https://doi.org/10.1175/JCLI319.1).
- , E. Guilyardi, G. Madec, J. Slingo, and S. Woolnough, 2007: Impact of resolving the diurnal cycle in an ocean–atmosphere GCM. Part 1: A diurnally forced OGCM. *Climate Dyn.*, **29**, 575–590, doi:[10.1007/s00382-007-0249-6](https://doi.org/10.1007/s00382-007-0249-6).
- , —, —, —, —, and J. Cole, 2008: Impact of resolving the diurnal cycle in an ocean–atmosphere GCM. Part 2: A diurnally coupled CGCM. *Climate Dyn.*, **31**, 909–925, doi:[10.1007/s00382-008-0429-z](https://doi.org/10.1007/s00382-008-0429-z).

- Bladé, I., and D. L. Hartmann, 1993: Tropical intraseasonal oscillation in a simple nonlinear model. *J. Atmos. Sci.*, **50**, 2922–2939, doi:10.1175/1520-0469(1993)050<2922:TIOIAS>2.0.CO;2.
- Bretherton, C. S., and S. Park, 2009: A new moist turbulence parameterization in the Community Atmosphere Model. *J. Climate*, **22**, 3422–3448, doi:10.1175/2008JCLI2556.1.
- Chen, F., and J. Dudhia, 2001: Coupling an advanced land surface-hydrology model with the Penn State–NCAR MM5 modeling system. Part I: Model implementation and sensitivity. *Mon. Wea. Rev.*, **129**, 569–585, doi:10.1175/1520-0493(2001)129<0569:CAALSH>2.0.CO;2.
- Chen, S. S., and R. A. Houze Jr., 1997: Diurnal variation and life cycle of deep convective systems over the tropical Pacific warm pool. *Quart. J. Roy. Meteor. Soc.*, **123**, 357–388, doi:10.1002/qj.49712353806.
- Chou, M.-D., and M. J. Suarez, 1999: A solar radiation parameterization for atmospheric studies. NASA Tech. Rep. NASA/TM-1999-104606, Vol. 15, 38 pp.
- Clayson, C. A., and A. S. Bogdanoff, 2013: The effect of diurnal sea surface temperature warming on climatological air–sea fluxes. *J. Climate*, **26**, 2546–2556, doi:10.1175/JCLI-D-12-00062.1.
- Cummings, J. A., 2005: Operational multivariate ocean data assimilation. *Quart. J. Roy. Meteor. Soc.*, **131**, 3583–3604, doi:10.1256/qj.05.105.
- Dee, D., and Coauthors, 2011: The ERA-Interim reanalysis: Configuration and performance of the data assimilation system. *Quart. J. Roy. Meteor. Soc.*, **137**, 553–597, doi:10.1002/qj.828.
- Del Genio, A. D., Y. Chen, D. Kim, and M.-S. Yao, 2012: The MJO transition from shallow to deep convection in *CloudSat/CALIPSO* and GISS GCM simulations. *J. Climate*, **25**, 3755–3770, doi:10.1175/JCLI-D-11-00384.1.
- Fairall, C., E. F. Bradley, J. Godfrey, G. Wick, J. Edson, and G. Young, 1996: Cool-skin and warm-layer effects on sea surface temperature. *J. Geophys. Res.*, **101**, 1295–1308, doi:10.1029/95JC03190.
- , —, J. Hare, A. Grachev, and J. Edson, 2003: Bulk parameterization of air–sea fluxes: Updates and verification for the COARE algorithm. *J. Climate*, **16**, 571–591, doi:10.1175/1520-0442(2003)016<0571:BPOASF>2.0.CO;2.
- Flatau, M., P. J. Flatau, P. Phoebeus, and P. P. Niiler, 1997: The feedback between equatorial convection and local radiative and evaporative processes: The implication for intraseasonal oscillations. *J. Atmos. Sci.*, **54**, 2373–2386, doi:10.1175/1520-0469(1997)054<2373:TFBECA>2.0.CO;2.
- Fu, X., J.-Y. Lee, P.-C. Hsu, H. Taniguchi, B. Wang, W. Wang, and S. Weaver, 2013: Multi-model MJO forecasting during DYNAMO/CINDY period. *Climate Dyn.*, **41**, 1067–1081, doi:10.1007/s00382-013-1859-9.
- Gottschalck, J., and Coauthors, 2010: A framework for assessing operational Madden–Julian oscillation forecasts: A CLIVAR MJO working group project. *Bull. Amer. Meteor. Soc.*, **91**, 1247–1258, doi:10.1175/2010BAMS2816.1.
- , P. E. Roundy, C. J. Schreck III, A. Vintzileos, and C. Zhang, 2013: Large-scale atmospheric and oceanic conditions during the 2011–12 DYNAMO field campaign. *Mon. Wea. Rev.*, **141**, 4173–4196, doi:10.1175/MWR-D-13-00022.1.
- Haertel, P. T., G. N. Kiladis, A. Denno, and T. M. Rickenbach, 2008: Vertical-mode decompositions of 2-day waves and the Madden–Julian oscillation. *J. Atmos. Sci.*, **65**, 813–833, doi:10.1175/2007JAS2314.1.
- Hagos, S., L. R. Leung, and J. Dudhia, 2011: Thermodynamics of the MJO in a regional model with constrained moisture. *J. Atmos. Sci.*, **68**, 1974–1989, doi:10.1175/2011JAS3592.1.
- Haidvogel, D. B., H. G. Arango, K. Hedstrom, A. Beckmann, P. Malanotte-Rizzoli, and A. F. Shchepetkin, 2000: Model evaluation experiments in the North Atlantic basin: Simulations in nonlinear terrain-following coordinates. *Dyn. Atmos. Oceans*, **32**, 239–281, doi:10.1016/S0377-0265(00)00049-X.
- Han, W., 2005: Origins and dynamics of the 90-day and 30–60-day variations in the equatorial Indian Ocean. *J. Phys. Oceanogr.*, **35**, 708–728, doi:10.1175/JPO2725.1.
- , J. P. McCreary, D. L. T. Anderson, and A. J. Mariano, 1999: Dynamics of the eastward surface jets in the equatorial Indian Ocean. *J. Phys. Oceanogr.*, **29**, 2191–2209, doi:10.1175/1520-0485(1999)029<2191:DOTESJ>2.0.CO;2.
- Hendon, H. H., B. Liebmann, M. Newman, J. D. Glick, and J. Schemm, 2000: Medium range forecast errors associated with active episodes of the Madden–Julian oscillation. *Mon. Wea. Rev.*, **128**, 69–86, doi:10.1175/1520-0493(2000)128<0069:MRFEAW>2.0.CO;2.
- Hung, M.-P., J.-L. Lin, W. Wang, D. Kim, T. Shinoda, and S. J. Weaver, 2013: MJO and convectively coupled equatorial waves simulated by CMIP5 climate models. *J. Climate*, **26**, 6185–6214, doi:10.1175/JCLI-D-12-00541.1.
- Jerlov, N. G., 1968: *Optical Oceanography*. Elsevier, 193 pp.
- Johnson, R. H., and P. E. Ciesielski, 2013: Structure and properties of Madden–Julian oscillations deduced from DYNAMO sounding arrays. *J. Atmos. Sci.*, **70**, 3157–3179, doi:10.1175/JAS-D-13-065.1.
- , T. M. Rickenbach, S. A. Rutledge, P. E. Ciesielski, and W. H. Schubert, 1999: Trimodal characteristics of tropical convection. *J. Climate*, **12**, 2397–2418, doi:10.1175/1520-0442(1999)012<2397:TCOTC>2.0.CO;2.
- Juang, H.-M. H., and M. Kanamitsu, 1994: The NMC nested regional spectral model. *Mon. Wea. Rev.*, **122**, 3–26, doi:10.1175/1520-0493(1994)122<0003:TNNRSM>2.0.CO;2.
- Kalnay, E., and Coauthors, 1996: The NCEP/NCAR 40-Year Reanalysis Project. *Bull. Amer. Meteor. Soc.*, **77**, 437–471, doi:10.1175/1520-0477(1996)077<0437:TNYRP>2.0.CO;2.
- Kawai, Y., and A. Wada, 2007: Diurnal sea surface temperature variation and its impact on the atmosphere and ocean: A review. *J. Oceanogr.*, **63**, 721–744, doi:10.1007/s10872-007-0063-0.
- Kemball-Cook, S. R., and B. C. Weare, 2001: The onset of convection in the Madden–Julian oscillation. *J. Climate*, **14**, 780–793, doi:10.1175/1520-0442(2001)014<0780:TOOCIT>2.0.CO;2.
- Kikuchi, K., and Y. N. Takayabu, 2004: The development of organized convection associated with the MJO during TOGA COARE IOP: Trimodal characteristics. *Geophys. Res. Lett.*, **31**, L10101, doi:10.1029/2004GL019601.
- Kiladis, G. N., K. H. Straub, and P. T. Haertel, 2005: Zonal and vertical structure of the Madden–Julian oscillation. *J. Atmos. Sci.*, **62**, 2790–2809, doi:10.1175/JAS3520.1.
- Kim, H.-M., P. J. Webster, V. E. Toma, and D. Kim, 2014: Predictability and prediction skill of the MJO in two operational forecasting systems. *J. Climate*, **27**, 5364–5378, doi:10.1175/JCLI-D-13-00480.1.
- Kiranmayi, L., and E. D. Maloney, 2011: The intraseasonal moist static energy budget in reanalysis data. *J. Geophys. Res.*, **116**, D21117, doi:10.1029/2011JD016031.
- Klingaman, N. P., P. M. Inness, H. Weller, and J. M. Slingo, 2008: The importance of high-frequency sea surface temperature variability to the intraseasonal oscillation of Indian monsoon rainfall. *J. Climate*, **21**, 6119–6140, doi:10.1175/2008JCLI2329.1.
- , S. J. Woolnough, H. Weller, and J. M. Slingo, 2011: The impact of finer-resolution air–sea coupling on the intraseasonal

- oscillation of the Indian monsoon. *J. Climate*, **24**, 2451–2468, doi:[10.1175/2010JCLI3868.1](https://doi.org/10.1175/2010JCLI3868.1).
- Large, W. G., J. C. McWilliams, and S. C. Doney, 1994: Oceanic vertical mixing: A review and a model with a nonlocal boundary layer parameterization. *Rev. Geophys.*, **32**, 363–403, doi:[10.1029/94RG01872](https://doi.org/10.1029/94RG01872).
- Li, Y., W. Han, T. Shinoda, C. Wang, R.-C. Lien, J. N. Moum, and J.-W. Wang, 2013: Effects of the diurnal cycle in solar radiation on the tropical Indian Ocean mixed layer variability during wintertime Madden–Julian oscillations. *J. Geophys. Res. Oceans*, **118**, 4945–4964, doi:[10.1002/jgrc.20395](https://doi.org/10.1002/jgrc.20395).
- Lin, J.-L., and Coauthors, 2006: Tropical intraseasonal variability in 14 IPCC AR4 climate models. Part I: Convective signals. *J. Climate*, **19**, 2665–2690, doi:[10.1175/JCLI3735.1](https://doi.org/10.1175/JCLI3735.1).
- Ling, J., P. Bauer, P. Bechtold, A. Beljaars, R. Forbes, F. Vitart, M. Ulate, and C. Zhang, 2014: Global versus local MJO forecast skill of the ECMWF model during DYNAMO. *Mon. Wea. Rev.*, **142**, 2228–2247, doi:[10.1175/MWR-D-13-00292.1](https://doi.org/10.1175/MWR-D-13-00292.1).
- Madden, R. A., and P. R. Julian, 1971: Detection of a 40–50 day oscillation in the zonal wind in the tropical Pacific. *J. Atmos. Sci.*, **28**, 702–708, doi:[10.1175/1520-0469\(1971\)028<0702:DOADOI>2.0.CO;2](https://doi.org/10.1175/1520-0469(1971)028<0702:DOADOI>2.0.CO;2).
- , and —, 1994: Observations of the 40–50-day tropical oscillation: A review. *Mon. Wea. Rev.*, **122**, 814–837, doi:[10.1175/1520-0493\(1994\)122<0814:OOTDTO>2.0.CO;2](https://doi.org/10.1175/1520-0493(1994)122<0814:OOTDTO>2.0.CO;2).
- , and —, 2005: Historical perspective. *Intraseasonal Variability in the Atmosphere–Ocean Climate System*, W. K.-M. Lau and D. Waliser, Eds., Springer-Praxis, 1–16.
- Maloney, E. D., 2009: The moist static energy budget of a composite tropical intraseasonal oscillation in a climate model. *J. Climate*, **22**, 711–729, doi:[10.1175/2008JCLI2542.1](https://doi.org/10.1175/2008JCLI2542.1).
- , and A. H. Sobel, 2004: Surface fluxes and ocean coupling the tropical intraseasonal oscillation. *J. Climate*, **17**, 4368–4386, doi:[10.1175/JCLI-3212.1](https://doi.org/10.1175/JCLI-3212.1).
- , —, and W. M. Hannah, 2010: Intraseasonal variability in an aquaplanet general circulation model. *J. Adv. Model. Earth Syst.*, **2** (5), doi:[10.3894/JAMES.2010.2.5](https://doi.org/10.3894/JAMES.2010.2.5).
- Mlawer, E. J., and S. A. Clough, 1997: On the extension of RRTM to the shortwave region. *Proc. Sixth Atmospheric Measurement (ARM) Science Team Meeting*, Washington, DC, U.S. Department of Energy, 223–226.
- Moum, J. N., and Coauthors, 2014: Air–sea interactions from westerly wind bursts during the November 2011 MJO in the Indian Ocean. *Bull. Amer. Meteor. Soc.*, **95**, 1185–1199, doi:[10.1175/BAMS-D-12-00225.1](https://doi.org/10.1175/BAMS-D-12-00225.1).
- Neale, R. B., J. H. Richter, and M. Jochum, 2008: The impact of convection on ENSO: From a delayed oscillator to a series of events. *J. Climate*, **21**, 5904–5924, doi:[10.1175/2008JCLI2244.1](https://doi.org/10.1175/2008JCLI2244.1).
- Park, S., and C. S. Bretherton, 2009: The University of Washington shallow convection and moist turbulence schemes and their impact on climate simulations with the Community Atmosphere Model. *J. Climate*, **22**, 3449–3469, doi:[10.1175/2008JCLI2557.1](https://doi.org/10.1175/2008JCLI2557.1).
- Putrasahan, D. A., A. J. Miller, and H. Seo, 2013a: Isolating mesoscale coupled ocean–atmosphere interactions in the Kurshio Extension region. *Dyn. Atmos. Oceans*, **63**, 60–78, doi:[10.1016/j.dynatmoce.2013.04.001](https://doi.org/10.1016/j.dynatmoce.2013.04.001).
- , —, and —, 2013b: Regional coupled ocean–atmosphere downscaling in the southeast Pacific: Impacts on upwelling, mesoscale air–sea fluxes, and ocean eddies. *Ocean Dyn.*, **63**, 463–488, doi:[10.1007/s10236-013-0608-2](https://doi.org/10.1007/s10236-013-0608-2).
- Ray, P., and C. Zhang, 2010: A case study of the mechanisms of extratropical influence on the initiation of the Madden–Julian oscillation. *J. Atmos. Sci.*, **67**, 515–528, doi:[10.1175/2009JAS3059.1](https://doi.org/10.1175/2009JAS3059.1).
- , and T. Li, 2013: Relative roles of circumnavigating waves and extratropics on the MJO and its relationship with the mean state. *J. Atmos. Sci.*, **70**, 876–893, doi:[10.1175/JAS-D-12-0153.1](https://doi.org/10.1175/JAS-D-12-0153.1).
- , C. Zhang, J. Dudhia, and S. S. Chen, 2009: A numerical case study on the initiation of the Madden–Julian oscillation. *J. Atmos. Sci.*, **66**, 310–331, doi:[10.1175/2008JAS2701.1](https://doi.org/10.1175/2008JAS2701.1).
- , —, M. W. Moncrieff, J. Dudhia, J. M. Caron, L. R. Leung, and C. Bruyere, 2011: Role of the atmospheric mean state on the initiation of the Madden–Julian oscillation in a tropical channel model. *Climate Dyn.*, **36**, 161–184, doi:[10.1007/s00382-010-0859-2](https://doi.org/10.1007/s00382-010-0859-2).
- Raymond, D. J., G. B. Raga, C. S. Bretherton, J. Molinari, C. Lopez-Carillo, and Z. Fuchs, 2003: Convective forcing in the intertropical convergence zone of the eastern Pacific. *J. Atmos. Sci.*, **60**, 2064–2082, doi:[10.1175/1520-0469\(2003\)060<2064:CFITIC>2.0.CO;2](https://doi.org/10.1175/1520-0469(2003)060<2064:CFITIC>2.0.CO;2).
- Schiller, A., and J. S. Godfrey, 2005: A diagnostic model of the diurnal cycle of sea surface temperature for use in coupled ocean–atmosphere models. *J. Geophys. Res.*, **110**, C11014, doi:[10.1029/2005JC002975](https://doi.org/10.1029/2005JC002975).
- Seo, H., and S.-P. Xie, 2011: Response and impact of equatorial ocean dynamics and tropical instability waves in the tropical Atlantic under global warming: A regional coupled downscaling study. *J. Geophys. Res.*, **116**, C03026, doi:[10.1029/2010JC006670](https://doi.org/10.1029/2010JC006670).
- , and —, 2013: Impact of ocean warm layer thickness on the intensity of Hurricane Katrina in a regional coupled model. *Meteor. Atmos. Phys.*, **122**, 19–32, doi:[10.1007/s00703-013-0275-3](https://doi.org/10.1007/s00703-013-0275-3).
- , M. Jochum, R. Murtugudde, and A. J. Miller, 2006: Effect of ocean mesoscale variability on the mean state of tropical Atlantic climate. *Geophys. Res. Lett.*, **33**, L09606, doi:[10.1029/2005GL025651](https://doi.org/10.1029/2005GL025651).
- , —, —, —, and J. O. Roads, 2007a: Feedback of tropical-instability wave-induced atmospheric variability onto the ocean. *J. Climate*, **20**, 5842–5855, doi:[10.1175/JCLI4330.1](https://doi.org/10.1175/JCLI4330.1).
- , A. J. Miller, and J. O. Roads, 2007b: The Scripps Coupled Ocean–Atmosphere Regional (SCOAR) model, with applications in the eastern Pacific sector. *J. Climate*, **20**, 381–402, doi:[10.1175/JCLI4016.1](https://doi.org/10.1175/JCLI4016.1).
- , M. Jochum, R. Murtugudde, A. J. Miller, and J. O. Roads, 2008a: Precipitation from African easterly waves in a coupled model of the tropical Atlantic. *J. Climate*, **21**, 1417–1431, doi:[10.1175/2007JCLI1906.1](https://doi.org/10.1175/2007JCLI1906.1).
- , R. Murtugudde, M. Jochum, and A. J. Miller, 2008b: Modeling of mesoscale coupled ocean–atmosphere interaction and its feedback to ocean in the western Arabian Sea. *Ocean Modell.*, **25**, 120–131, doi:[10.1016/j.ocemod.2008.07.003](https://doi.org/10.1016/j.ocemod.2008.07.003).
- , S.-P. Xie, R. Murtugudde, M. Jochum, and A. J. Miller, 2009: Seasonal effects of Indian Ocean freshwater forcing in a regional coupled model. *J. Climate*, **22**, 6577–6596, doi:[10.1175/2009JCLI2990.1](https://doi.org/10.1175/2009JCLI2990.1).
- Seo, K.-H., and W. Wang, 2010: The Madden–Julian oscillation simulated in the NCEP Climate Forecast System Model: The importance of stratiform heating. *J. Climate*, **23**, 4770–4793, doi:[10.1175/2010JCLI2983.1](https://doi.org/10.1175/2010JCLI2983.1).
- , —, J. Gottschalck, Q. Zhang, J.-K. E. Schemm, W. R. Higgins, and A. Kumar, 2009: Evaluation of MJO forecast skill from several statistical and dynamical forecast models. *J. Climate*, **22**, 2372–2388, doi:[10.1175/2008JCLI2421.1](https://doi.org/10.1175/2008JCLI2421.1).

- Shchepetkin, A. F., and J. C. McWilliams, 2005: The Regional Oceanic Modeling System (ROMS): A split-explicit, free-surface, topography-following-coordinate ocean model. *Ocean Model.*, **9**, 347–404, doi:[10.1016/j.ocemod.2004.08.002](https://doi.org/10.1016/j.ocemod.2004.08.002).
- Shinoda, T., 2005: Impact of the diurnal cycle of solar radiation on intraseasonal SST variability in the western equatorial Pacific. *J. Climate*, **18**, 2628–2636, doi:[10.1175/JCLI3432.1](https://doi.org/10.1175/JCLI3432.1).
- , and H. H. H. Hendon, 1998: Mixed layer modeling of intraseasonal variability in the tropical western Pacific and Indian Oceans. *J. Climate*, **11**, 2668–2685, doi:[10.1175/1520-0442\(1998\)011<2668:MLMOIV>2.0.CO;2](https://doi.org/10.1175/1520-0442(1998)011<2668:MLMOIV>2.0.CO;2).
- , T. Jensen, M. Flatau, and S. Chen, 2013: Surface wind and upper-ocean variability associated with the Madden–Julian oscillation simulated by the Coupled Ocean–Atmosphere Mesoscale Prediction System (COAMPS). *Mon. Wea. Rev.*, **141**, 2290–2307, doi:[10.1175/MWR-D-12-00273.1](https://doi.org/10.1175/MWR-D-12-00273.1).
- Skamarock, W. C., and Coauthors, 2008: A description of the Advanced Research WRF version 3. NCAR Tech. Rep. NCAR/TN-475+STR, 113 pp, doi:[10.5065/D68S4MVH](https://doi.org/10.5065/D68S4MVH).
- Slingo, J., P. Inness, R. Neale, S. Woolnough, and G.-Y. Yang, 2003: Scale interactions on diurnal to seasonal timescales and their relevance to model systematic errors. *Ann. Geophys.*, **46**, 139–155, doi:[10.4401/ag-3383](https://doi.org/10.4401/ag-3383).
- Sobel, A. H., E. D. Maloney, G. Bellon, and D. M. Frierson, 2008: The role of surface heat fluxes in tropical intra-seasonal oscillations. *Nat. Geosci.*, **1**, 653–657, doi:[10.1038/ngeo312](https://doi.org/10.1038/ngeo312).
- Stephens, G. L., P. J. Webster, R. H. Johnson, R. Engelen, and T. S. L'Eucyer, 2004: Observational evidence for the mutual regulation of the tropical hydrological cycle and the tropical sea surface temperatures. *J. Climate*, **17**, 2213–2224, doi:[10.1175/1520-0442\(2004\)017<2213:OEFTMR>2.0.CO;2](https://doi.org/10.1175/1520-0442(2004)017<2213:OEFTMR>2.0.CO;2).
- Straub, K. H., 2013: MJO initiation in the real-time multivariate MJO index. *J. Climate*, **26**, 1130–1151, doi:[10.1175/JCLI-D-12-00074.1](https://doi.org/10.1175/JCLI-D-12-00074.1).
- Subramanian, A. C., M. Jochum, A. J. Miller, R. Murtugudde, R. B. Neale, and D. E. Waliser, 2011: The Madden–Julian oscillation in CCSM4. *J. Climate*, **24**, 6261–6282, doi:[10.1175/JCLI-D-11-00031.1](https://doi.org/10.1175/JCLI-D-11-00031.1).
- Sui, C.-H., X. Li, K.-M. Lau, and D. Adamec, 1997: Multiscale air–sea interactions during TOGA COARE. *Mon. Wea. Rev.*, **125**, 448–462, doi:[10.1175/1520-0493\(1997\)125<0448:MASIDT>2.0.CO;2](https://doi.org/10.1175/1520-0493(1997)125<0448:MASIDT>2.0.CO;2).
- Thayer-Calder, K., and D. A. Randall, 2009: The role of convective moistening in the Madden–Julian oscillation. *J. Atmos. Sci.*, **66**, 3297–3312, doi:[10.1175/2009JAS3081.1](https://doi.org/10.1175/2009JAS3081.1).
- Vitart, F., and T. Jung, 2010: Impact of the Northern Hemisphere extratropics on the skill in predicting the Madden Julian Oscillation. *Geophys. Res. Lett.*, **37**, L23805, doi:[10.1029/2010GL045465](https://doi.org/10.1029/2010GL045465).
- , and F. Molteni, 2010: Simulation of the Madden–Julian oscillation and its teleconnections in the ECMWF forecast system. *Quart. J. Roy. Meteor. Soc.*, **136**, 842–855, doi:[10.1002/qj.623](https://doi.org/10.1002/qj.623).
- Waliser, D. E., K. M. Lau, and J. H. Kim, 1999: The influence of coupled sea surface temperatures on the Madden–Julian oscillation: A model perturbation experiment. *J. Atmos. Sci.*, **56**, 333–358, doi:[10.1175/1520-0469\(1999\)056<0333:TIOCSS>2.0.CO;2](https://doi.org/10.1175/1520-0469(1999)056<0333:TIOCSS>2.0.CO;2).
- , R. Murtugudde, and L. E. Lucas, 2003: Indo-Pacific Ocean response to atmospheric intraseasonal variability: 1. Austral summer and the Madden–Julian oscillation. *J. Geophys. Res.*, **108**, 3160, doi:[10.1029/2002JC001620](https://doi.org/10.1029/2002JC001620).
- , and Coauthors, 2009: MJO simulation diagnostics. *J. Climate*, **22**, 3006–3030, doi:[10.1175/2008JCLI2731.1](https://doi.org/10.1175/2008JCLI2731.1).
- Webster, P. J., C. A. Clayson, and J. A. Curry, 1996: Clouds, radiation, and the diurnal cycle of sea surface temperature in the tropical western Pacific Ocean. *J. Climate*, **9**, 1712–1730, doi:[10.1175/1520-0442\(1996\)009<1712:CRATDC>2.0.CO;2](https://doi.org/10.1175/1520-0442(1996)009<1712:CRATDC>2.0.CO;2).
- Wedi, N., and P. K. Smolarkiewicz, 2010: A nonlinear perspective on the dynamics of the MJO: Idealized large-eddy simulations. *J. Atmos. Sci.*, **67**, 1202–1217, doi:[10.1175/2009JAS3160.1](https://doi.org/10.1175/2009JAS3160.1).
- Weller, R. A., and S. P. Anderson, 1996: Surface meteorology and air–sea fluxes in the western equatorial Pacific warm pool during the TOGA Coupled Ocean–Atmosphere Response Experiment. *J. Climate*, **9**, 1959–1990, doi:[10.1175/1520-0442\(1996\)009<1959:SMAASF>2.0.CO;2](https://doi.org/10.1175/1520-0442(1996)009<1959:SMAASF>2.0.CO;2).
- Wheeler, M., and H. Hendon, 2004: An all-season real-time multivariate MJO index: Development of an index for monitoring and prediction. *Mon. Wea. Rev.*, **132**, 1917–1932, doi:[10.1175/1520-0493\(2004\)132<1917:AARMMI>2.0.CO;2](https://doi.org/10.1175/1520-0493(2004)132<1917:AARMMI>2.0.CO;2).
- Woolnough, S. J., J. M. Slingo, and B. J. Hoskins, 2000: The relationship between convection and sea surface temperature on intraseasonal time scales. *J. Climate*, **13**, 2086–2104, doi:[10.1175/1520-0442\(2000\)013<2086:TRBCAS>2.0.CO;2](https://doi.org/10.1175/1520-0442(2000)013<2086:TRBCAS>2.0.CO;2).
- , —, and —, 2001: The organization of tropical convection by intraseasonal sea surface temperature anomalies. *Quart. J. Roy. Meteor. Soc.*, **127**, 887–907, doi:[10.1002/qj.49712757310](https://doi.org/10.1002/qj.49712757310).
- , F. Vitart, and M. Balmaseda, 2007: The role of the ocean in the Madden–Julian oscillation: Implications for MJO prediction. *Quart. J. Roy. Meteor. Soc.*, **133**, 117–128, doi:[10.1002/qj.4](https://doi.org/10.1002/qj.4).
- Xu, W., and S. A. Rutledge, 2014: Convective characteristics of the Madden–Julian oscillation over the central Indian Ocean observed by shipborne radar during DYNAMO. *J. Atmos. Sci.*, **71**, 2859–2877, doi:[10.1175/JAS-D-13-0372.1](https://doi.org/10.1175/JAS-D-13-0372.1).
- Yoneyama, K., C. Zhang, and C. N. Long, 2013: Tracking pulses of the Madden–Julian oscillation. *Bull. Amer. Meteor. Soc.*, **94**, 1871–1891, doi:[10.1175/BAMS-D-12-00157.1](https://doi.org/10.1175/BAMS-D-12-00157.1).
- Yoon, J.-H., 1981: Effects of islands on equatorial waves. *J. Geophys. Res.*, **86**, 10 913–10 920, doi:[10.1029/JC086iC11p10913](https://doi.org/10.1029/JC086iC11p10913).
- Yu, L., and R. A. Weller, 2007: Objectively Analyzed Air–Sea Heat Fluxes (OAFlux) for the global ice-free oceans. *Bull. Amer. Meteor. Soc.*, **88**, 527–539, doi:[10.1175/BAMS-88-4-527](https://doi.org/10.1175/BAMS-88-4-527).
- Zhang, C., 2005: Madden–Julian oscillation. *Rev. Geophys.*, **43**, RG2003, doi:[10.1029/2004RG000158](https://doi.org/10.1029/2004RG000158).
- , 2013: Madden–Julian oscillation: Bridging weather and climate. *Bull. Amer. Meteor. Soc.*, **94**, 1849–1870, doi:[10.1175/BAMS-D-12-00026.1](https://doi.org/10.1175/BAMS-D-12-00026.1).
- , and S. P. Anderson, 2003: Sensitivity of intraseasonal perturbations in SST to the structure of the MJO. *J. Atmos. Sci.*, **60**, 2196–2207, doi:[10.1175/1520-0469\(2003\)060<2196:SOIPIS>2.0.CO;2](https://doi.org/10.1175/1520-0469(2003)060<2196:SOIPIS>2.0.CO;2).
- , M. Dong, S. Gualdi, H. H. Hendon, E. D. Maloney, A. Marshall, K. R. Sperber, and W. Wang, 2006: Simulations of the Madden–Julian oscillation by four pairs of coupled and uncoupled global models. *Climate Dyn.*, **27**, 573–592, doi:[10.1007/s00382-006-0148-2](https://doi.org/10.1007/s00382-006-0148-2).
- Zhang, G. J., and N. A. McFarlane, 1995: Sensitivity of climate simulations to the parameterization of cumulus convection in the Canadian Climate Centre general circulation model. *Atmos.–Ocean*, **33**, 407–446, doi:[10.1080/07055900.1995.9649539](https://doi.org/10.1080/07055900.1995.9649539).
- Zhou, L., R. B. Neale, M. Jochum, and R. Murtugudde, 2012: Improved Madden–Julian oscillations with improved physics: The impact of modified convection parameterizations. *J. Climate*, **25**, 1116–1136, doi:[10.1175/2011JCLI4059.1](https://doi.org/10.1175/2011JCLI4059.1).